Cell Reports

Article

Decoupling astrocytes in adult mice impairs synaptic plasticity and spatial learning

Graphical abstract

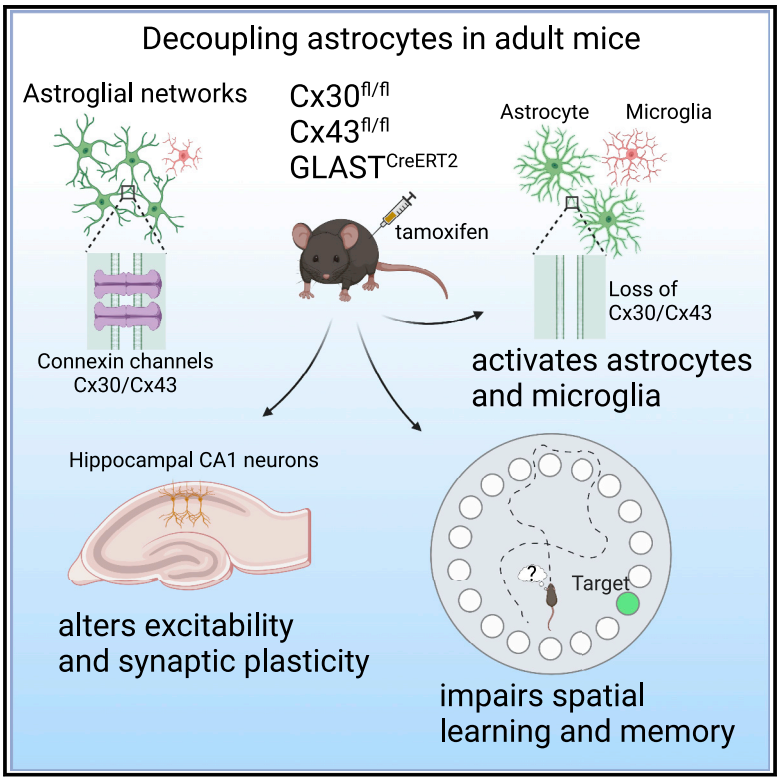

Highlights

- Inducible deletion of Cx30 and Cx43 disrupts astrocytic coupling in adult mice
- Loss of astrocytic connexins and coupling activate astrocytes and microglia
- Astroglial networks control hippocampal synaptic transmission and plasticity
- Disrupting astroglial coupling impairs spatial learning and memory

Authors

Ladina Hösli, Noemi Binini, Kim David Ferrari, ..., Christian Giaume, Bruno Weber, Aiman S. Saab

Correspondence

bweber@pharma.uzh.ch (B.W.), asaab@pharma.uzh.ch (A.S.S.)

In brief

Astrocytes form large intercellular networks by gap junction coupling, but the functional importance of astrocytic coupling in adult mice remains poorly explored. Hösli et al. report that astroglial networks in the adult brain are vital for neural homeostasis, hippocampal plasticity, and spatial cognition.

Hösli et al., 2022, Cell Reports *38*, 110484
March 8, 2022
https://doi.org/10.1016/j.celrep.2022.110484

CellPress

Cell Reports

CellPress
OPEN ACCESS

Article

Decoupling astrocytes in adult mice impairs synaptic plasticity and spatial learning

Ladina Hösli,[1,2] Noemi Binini,[1,2] Kim David Ferrari,[1,2] Laetitia Thieren,[1,2] Zoe J. Looser,[1,2] Marc Zuend,[1,2] Henri S. Zanker,[1,2] Stewart Berry,[3,7] Martin Holub,[1,2,6] Wiebke Möbius,[4] Torben Ruhwedel,[4] Klaus-Armin Nave,[4] Christian Giaume,[5,7] Bruno Weber,[1,2,*] and Aiman S. Saab[1,2,8,*]

[1]Institute of Pharmacology and Toxicology, University of Zurich, 8057 Zurich, Switzerland
[2]Neuroscience Center Zurich, University and ETH Zurich, 8057 Zurich, Switzerland
[3]Brain Research Institute, University of Zurich, 8057 Zurich, Switzerland
[4]Max Planck Institute of Experimental Medicine, 37075 Göttingen, Germany
[5]Center for Interdisciplinary Research in Biology (CIRB), Collège de France, 75231 Paris Cedex 05, France
[6]Present address: Department of Bionanoscience, TU Delft, Delft 2629, the Netherlands
[7]Dedicated to the memory of Stewart Berry and Christian Giaume
[8]Lead contact
*Correspondence: bweber@pharma.uzh.ch (B.W.), asaab@pharma.uzh.ch (A.S.S.)
https://doi.org/10.1016/j.celrep.2022.110484

SUMMARY

The mechanisms by which astrocytes modulate neural homeostasis, synaptic plasticity, and memory are still poorly explored. Astrocytes form large intercellular networks by gap junction coupling, mainly composed of two gap junction channel proteins, connexin 30 (Cx30) and connexin 43 (Cx43). To circumvent developmental perturbations and to test whether astrocytic gap junction coupling is required for hippocampal neural circuit function and behavior, we generate and study inducible, astrocyte-specific Cx30 and Cx43 double knockouts. Surprisingly, disrupting astrocytic coupling in adult mice results in broad activation of astrocytes and microglia, without obvious signs of pathology. We show that hippocampal CA1 neuron excitability, excitatory synaptic transmission, and long-term potentiation are significantly affected. Moreover, behavioral inspection reveals deficits in sensorimotor performance and a complete lack of spatial learning and memory. Together, our findings establish that astrocytic connexins and an intact astroglial network in the adult brain are vital for neural homeostasis, plasticity, and spatial cognition.

INTRODUCTION

Neurons and astrocytes cultivate a highly dynamic dialogue with each other that is critical for normal brain function. Astrocytes are involved in a plethora of homeostatic processes, ranging from the regulation and modulation of synaptic transmission (Araque et al., 1999; Santello et al., 2019), neurotransmitter, ionic and energy homeostasis (Magistretti and Allaman, 2018; Weber and Barros, 2015), to network plasticity and cognitive abilities (Adamsky and Goshen, 2018; Suzuki et al., 2011). Astrocytes are highly interconnected and organized in large networks via gap junction channels composed of connexin 30 (Cx30) and connexin 43 (Cx43) (Giaume et al., 2010; Pannasch et al., 2011; Theis et al., 2005). This astroglial channel network allows for intercellular communication, trafficking, and redistribution of various neuroactive molecules, such as ions, neurotransmitters, and metabolites (Giaume et al., 2010).

Most of our current ideas on the function of the astroglial network are obtained from research in mice in which Cx30 and Cx43 were inactivated during brain development (Pannasch and Rouach, 2013). These double-deficient mice have been generated by crossing Cx30 *null* mutants (Teubner et al., 2003) with mice having a conditional Cx43 deletion in astrocytes (Theis et al., 2003), driven by embryonically or perinatally active Cre transgenic lines under the control of the human glial fibrillary acidic protein promoter (hGFAP-Cre) (Zhuo et al., 2001) or the murine GFAP promoter (mGFAP-Cre) (Garcia et al., 2004). Postnatal studies in *Cx30*$^{-/-}$*:Cx43*$^{fl/fl}$*:hGFAP-Cre* mice showed that a lack of astrocytic connexin hemichannels and gap junctions in the developing brain produces defects in synaptic plasticity and network excitability, extracellular potassium and glutamate homeostasis, and in nutrient supply to neurons (Chever et al., 2016; Pannasch et al., 2011, 2012; Rouach et al., 2008; Wallraff et al., 2006). Moreover, early-onset dysmyelination, axonal pathology, and the formation of vacuoles in gray and white matter are striking features of *Cx30*$^{-/-}$*:Cx43*$^{fl/fl}$*:mGFAP-Cre* mice (Lutz et al., 2009). Similar white matter pathology and myelin vacuolation were observed in mice deficient in the oligodendroglial connexins Cx32 and Cx47 (Menichella et al., 2003, 2006), suggesting that a lack of functional gap junction coupling between astrocytes and oligodendrocytes (Magnotti et al., 2011; Orthmann-Murphy et al., 2007; Rash, 2010) causes abnormal white matter development that disrupts axonal integrity.

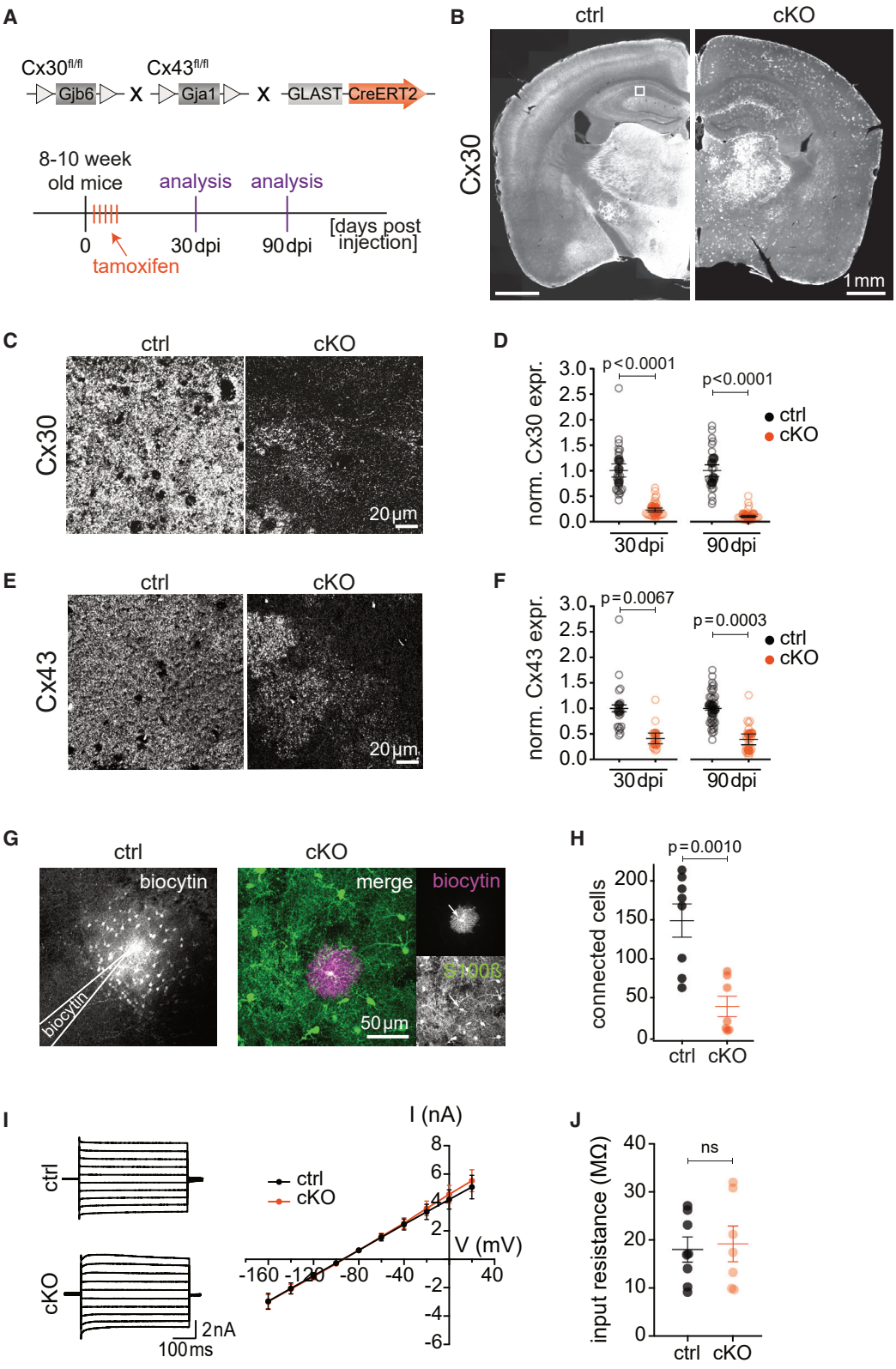

(legend on next page)

Having numerous functions in development, Cx30 and Cx43 play a role in cell migration, proliferation, and differentiation (Cina et al., 2009; Elias et al., 2007; Ghézali et al., 2018; Kunze et al., 2009; Lagos-Cabré et al., 2019). For instance, Cx43 in radial glial cells promotes neuronal migration and neocortical laminar formation during development (Cina et al., 2009; Elias et al., 2007). Cx30 contributes to astroglial polarization during postnatal maturation (Ghézali et al., 2018), and Cx30-deficient mice show impaired cochlear development and severe hearing loss (Cohen-Salmon et al., 2007; Teubner et al., 2003). Furthermore, depending on the genetic background of the mice, hGFAP-Cre-mediated, embryonic deletion of Cx43 impairs cellular organization of the cortex, hippocampus, and cerebellum (Wiencken-Barger et al., 2007).

To disentangle these developmental connexin attributes in Cx30- and Cx43-deficient mice from the later functional role of the astroglial gap junction network in the adult brain, we generated and studied inducible, astrocyte-specific Cx30 and Cx43 conditional knockout (cKO) mice. Interestingly, loss of astrocytic connexins and network coupling in the adult brain led to a widespread astrocyte and microglia activation, an unexpected finding that was unrelated to tissue damage or neural loss. However, we found that hippocampal CA1 neuron excitability was reduced while excitatory synaptic transmission was enhanced. The induction of long-term potentiation in CA1 was also compromised, possibly due to alterations in D-serine homeostasis. In addition, hippocampus-dependent spatial learning and memory was severely impaired in cKO mice. Thus, our findings demonstrate that an intact astroglial network is critical for neural homeostasis, circuit functions, and cognitive abilities in the adult brain.

RESULTS

Inducible deletion of Cx30 and Cx43 impairs astrocytic gap junction coupling

To study the role of astrocytic gap junction coupling in adult mice, we generated inducible double knockouts to selectively delete Cx30 and Cx43 from astrocytes. We crossbred mice carrying loxP-flanked *Gjb6* ($Cx30^{fl/fl}$ mice; Boulay et al., 2013) and *Gja1* ($Cx43^{fl/fl}$ mice; Theis et al., 2003) alleles with mice expressing the Cre-recombinase CreERT2 under the GLAST(*Slc1a3*) promoter (Mori et al., 2006; Figure 1A). Adult, 8- to 10-week-old mice ($Cx30^{fl/fl}$:$Cx43^{fl/fl}$:$GLAST^{CreERT2/+}$, termed cKO) were treated with tamoxifen for 5 consecutive days, and Cx30 and Cx43 deletion was studied at 30 and 90 days post-injection (dpi, Figure 1A). Littermate control mice ($Cx30^{fl/fl}$:$Cx43^{fl/fl}$:$GLAST^{+/+}$) were identically treated. At 30 dpi, we determined a significant reduction in *Gjb6* and *Gja1* mRNA expression from both gray- and white-matter-enriched brain regions (Figures S1A and S1B). Immunostainings confirmed a clear loss of Cx30 and Cx43 expression in cKO mice at 30 and 90 dpi, as shown for hippocampus and cortex (Figures 1B–1F and S1C–S1F). We observed the typical punctate staining pattern of astrocytic Cx30 and Cx43 throughout the brain of controls, whereas in cKO brains, only a few astrocytes remained visible still expressing connexins (Figures 1C, 1E, S1C, S1E, and S1G). These astrocytes were likely not targeted for recombination, as seen by GLAST-CreERT2-mediated reporter expression (Figure S1H). We quantified the loss of Cx30 and Cx43 by confocal analysis in hippocampal CA1 (Figures 1C–1F) and the somatosensory cortex (Figures S1C–S1F). In the hippocampus, at 90 dpi, Cx30 and Cx43 expression was significantly reduced by 90% ± 12% (Figure 1D; $p < 0.0001$) and by 61% ± 11% (Figure 1F; $p = 0.0003$), respectively. A similar degree of Cx30 and Cx43 deletion was observed in the cortex (Figures S1C–S1F).

Given the residual expression of connexins, we next examined the extent to which astrocytic gap junction coupling is impaired in cKO mice. For this, we performed dye coupling experiments around 90 dpi in acute hippocampal slices (Figures 1G and 1H). Intercellular coupling assessed by biocytin diffusion was found to be significantly reduced by 74% ± 17% ($p = 0.0010$; Figure 1H), without overt changes in the intrinsic membrane properties of whole-cell patched astrocytes from both genotypes (Figures 1I and 1J).

Astrocytic decoupling leads to activation of astrocytes and microglia

Developmental loss of Cx30 and Cx43 causes severe hippocampal CA1 vacuolation and white matter pathology (Lutz et al.,

Figure 1. Inducible disruption of astroglial gap-junction coupling in adult mice

(A) Generation of $Cx30^{fl/fl}$:$Cx43^{fl/fl}$:$GLAST^{CreERT2/+}$ mice. Tamoxifen treatment in 8- to 10-week-old mice and analysis was performed at 30 and 90 days post-injection (dpi).

(B) Overview images of Cx30 immunolabeled coronal sections from control (ctrl) and cKO at 90 dpi. White box indicates example region used for quantifications, depicted in (C) and (E).

(C and D) Confocal images showing Cx30 in CA1 of ctrl and cKO mice at 90 dpi (C) and quantification of Cx30 expression (D). Compared with ctrl, Cx30 expression in cKO mice was reduced by 78% ± 13% at 30 dpi ($n = 3–4$; $N = 27–36$; $r = 4.82$; $t(13.0) = 6.98$; $p < 0.0001$) and by 90% ± 12% at 90 dpi ($n = 4–5$; $N = 24–27$; $r = 11.33$; $t(21.9) = 10.66$; $p < 0.0001$).

(E and F) Confocal images showing Cx43 in CA1 of ctrl and cKO mice at 90 dpi (E) and quantification of Cx43 expression (F). Compared with ctrl, Cx43 expression in cKO mice was reduced by 59% ± 12% at 30 dpi ($n = 2$; $N = 18$; $r = 2.28$; $t(11.81) = 3.28$; $p = 0.0067$) and by 61% ± 11% at 90 dpi ($n = 3–4$; $N = 27–36$; $r = 3.04$; $t(9.51) = 5.42$; $p = 0.0003$).

(G and H) Biocytin filling of astrocytes in hippocampal slices. (G) Example images (maximum projections) from ctrl (left) and cKO mice (right) co-stained with the astrocytic marker S100β are shown. (H) Quantification of biocytin-coupled cells revealed a reduction of 74% ± 17% in cKO mice compared with ctrl ($m = 7–8$; $t(11.4) = 4.40$; $p = 0.001$; unpaired t test).

(I and J) No difference was found in current-voltage (I/V) plots (I) and input resistance (J) in astrocytes from ctrl and cKO mice ($m = 7–8$; $t(10.1) = -0.27$; $p = 0.7875$; unpaired t test). ns, not significant.

Data are presented as mean ± SEM. Solid and empty circles (D and F) represent animal averages and all images quantified, respectively. m, number of cells from 4 to 5 animals per genotype; n, number of animals; N, number of images. Significance was tested using linear mixed effects models with post-hoc pairwise comparisons.

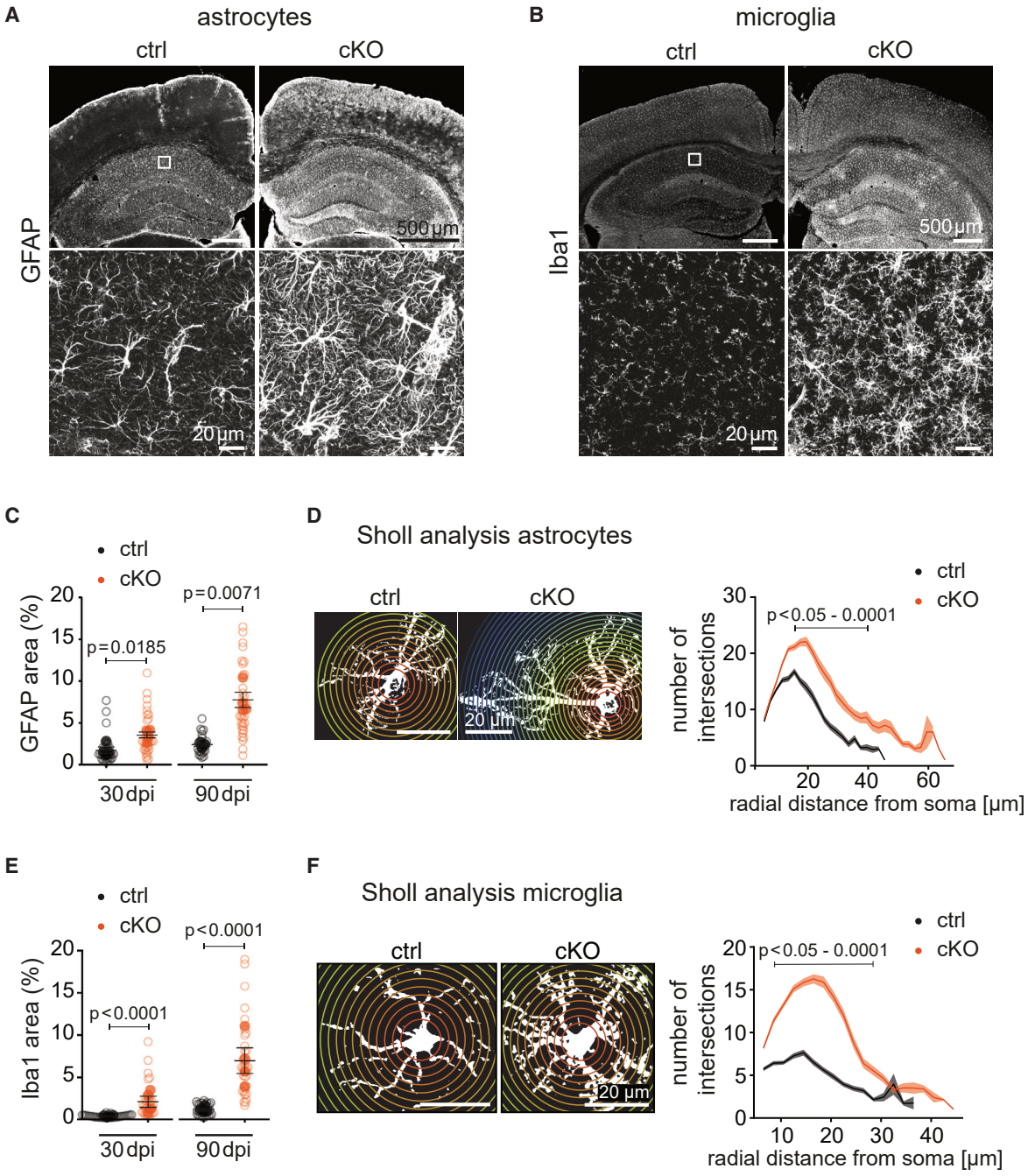

Figure 2. Activated astrocytes and microglia following decoupling of astrocytes

(A) Representative confocal images of GFAP immunolabeling from ctrl and cKO brain sections at 90 dpi. White box indicates magnified area depicted in lower panel.

(B) Representative confocal images of Iba1 staining from ctrl and cKO sections at 90 dpi. White box indicates magnified area depicted in lower panel.

(C) Quantification of GFAP-positive area in hippocampus. Compared with ctrl, cKO mice showed a significant increase in GFAP area at 30 dpi (n = 4; N = 36; r = 0.46; t(24.4) = −2.53; p = 0.0185) and at 90 dpi (n = 3–4; N = 27–36; r = 0.39; t(28.3) = −2.90; p = 0.0071).

(D) Sholl analysis of astrocytes at 90 dpi. Example of flattened and binarized GFAP-labeled astrocytes from ctrl and cKO mice with superimposed concentric circles used for analysis is shown (left panel). Quantification of the number of intersections is shown (right panel). Compared with astrocytes form ctrl mice (n = 3; M = 115), astrocytes from cKO mice showed significantly more intersections within circles ranging from 13.5 to 41.5 µm from the soma (n = 3; M = 81; $\chi^2(21) = 200.4$; $p < 0.0001$).

(legend continued on next page)

2009). We hence examined whether disruption of the astroglial network in adulthood affects cellular integrity or causes pathology. In coronal brain sections from cKO mice, we observed, both in gray and white matter regions, an increased immunoreactivity against the astrocytic marker GFAP (Figures 2A, 2C, and S2A–S2D) and the microglial marker Iba1 (Figures 2B, 2E, and S2E–S2H), indicative of activated astrocytes and microglia, respectively. Glial activation was already visible at 30 dpi and became more pronounced around 90 dpi (Figures 2C, 2E, and S2). Sholl analysis revealed that astrocytes and microglia became more ramified with more elongated processes (Figures 2D, 2F, and S3). However, astrocyte and microglia densities were unchanged (Figure S4), suggesting that glial activation in cKO mice was not accompanied by proliferation but primarily involved hypertrophy of resident astrocytes and microglia (Figures 2 and S3).

To further explore molecular changes associated with astrocytic decoupling, we performed tandem mass tag (TMT)-based quantitative proteomics analysis on hippocampal lysates (Figures 3A and 3B; Table S1). We detected an elevated protein abundance in GFAP, vimentin, and allograft inflammatory factor 1 (AIF1) (also known as Iba1) in cKO mice (Figure 3C), in line with our immunohistochemistry data (Figure 2). Notably, among the upregulated proteins in cKO mice, we identified four proteins (gene names *Iigp1*, *H2-D1*, *Psmb8*, and *Gbp2*; Figure 3C) previously ascribed to neuroinflammatory (A1-like) reactive astrocytes induced by microglia-secreted cytokines (Clarke et al., 2018; Liddelow et al., 2017). Indeed, gene set enrichment analysis (GSEA) and pathway analyses showed an overall increase in pro-inflammatory pathways in cKO mice, including elevated cytokine signaling, complement activation, antigen presentation, and phagocytosis-related processes (Figures 3D–3F). For example, GSEA pathway analysis revealed an increase in C-type lectin domain containing 7A (CLEC7A) signaling in cKO mice, which is indicative of pro-inflammatory microglia activation (Butovsky and Weiner, 2018; Krasemann et al., 2017). In fact, we validated the expression of CLEC7A in microglia of cKO mice with immunohistochemistry (Figure S5). Moreover, we found that CLEC7A expression associated with a clear reduction in the microglial homeostatic purinergic receptor P2RY12 (Figure S5), both of which are known microglial changes linked to disease-associated microglia (DAM) identified in various neurodegenerative diseases and the aging brain (Butovsky and Weiner, 2018; Hickman et al., 2013; Keren-Shaul et al., 2017). Thus, reduction of connexins and astrocytic decoupling in adult mice results in a pro-inflammatory-like activation of astrocytes and microglia.

However, despite the obvious glial activation in cKO mice, we found no apparent signs of tissue damage, such as cellular vacuolation (Figure S6A), a previously reported phenotype of developmental double-deficient *Cx30*$^{-/-}$*:Cx43*$^{fl/fl}$*:mGFAP-Cre* mice (Lutz et al., 2009). The gross architecture and structural organization of neuronal layers in the hippocampus appeared normal (Figures S6A and S6B). Moreover, neuronal (NeuN^{+}) cell densities in hippocampal CA1 or somatosensory cortex were unchanged (Figure S6C), suggesting no apparent neuronal loss in cKO mice. Indeed, we confirmed the absence of neurodegeneration by Fluoro-Jade C staining (Figure S6D), commonly used to detect degenerating neurons (Chao et al., 2019; Schmued et al., 1997). We further inspected whether synaptic loss occurred, given that inflammatory gliosis may lead to synaptic stripping (Butovsky and Weiner, 2018; Kettenmann et al., 2013; Salter and Stevens, 2017). However, ultrastructural analysis of CA1 stratum radiatum showed no difference in synaptic density between the genotypes (Figure S6E). Moreover, in contrast to previous observations in developmental *Cx30*$^{-/-}$*:Cx43*$^{fl/fl}$*:mGFAP-Cre* mice (Lutz et al., 2009), we observed no signs of demyelination or myelinic or axonal injury in adult cKO mice (Figure S7).

Taken together, decoupling astrocytes in adult mice led to a widespread glial activation, an exciting finding that was not associated with a visible pathology, such as vacuole formation, neuronal, synaptic, or myelin loss.

Changes in CA1 synaptic transmission and cell excitability in cKO mice

Previous studies in *Cx30*$^{-/-}$*:Cx43*$^{fl/fl}$*:hGFAP-Cre* mice reported (in ~2-week-old mice) that astrocytic connexins and gap junction coupling are involved in regulating neuronal excitability and synaptic physiology (Pannasch and Rouach, 2013; Pannasch et al., 2011). We hence examined how hippocampal neurotransmission and neuronal activity were affected by astrocytic decoupling in adult mice. Electrophysiological recordings from CA1 Schaffer collateral synapses and pyramidal neurons were performed in acute hippocampal slices between 80 and 120 dpi.

We inspected basal synaptic transmission by evoking field excitatory postsynaptic potentials (fEPSPs) in CA1 and evaluated the input-output properties (Figure S8). The presynaptic fiber volley amplitudes (inputs) in response to electrical stimulations were comparable between the genotypes. However, the slopes of the evoked fEPSPs (outputs) were reduced in cKO mice (Figure S8). Before further examining changes in synaptic transmission, we investigated the intrinsic membrane properties of CA1 pyramidal cells and found no difference in resting membrane potential or input resistance between the genotypes (Figures 4A and 4B). However, when testing excitability with current injection steps, pyramidal cells from cKO mice showed a reduced excitability evident from lower firing rates in response to depolarizing current pulses (Figures 4C and 4D). This is also reflected in an increased rheobase, the minimal current required to evoke action potentials (Figure 4E), but there were no changes in action potential amplitudes or threshold (Figures 4F and 4G).

(E) Quantification of Iba1-positive area in hippocampus. Compared with ctrl, cKO mice showed an increase in Iba1 area at 30 dpi ($n = 4$; $N = 36$; $r = 0.24$; $t(14.7) = -5.71$; $p < 0.0001$) and at 90 dpi ($n = 4$; $N = 36$; $r = 0.17$; $t(14.7) = -7.81$; $p < 0.0001$).

(F) Sholl analysis of microglia at 90 dpi and quantification of the number of intersections. Compared with microglia form ctrl mice ($n = 3$; $M = 64$), microglia from cKO mice showed significantly more intersections within circles ranging from 8 to 28 μm from the soma ($n = 3$; $M = 82$; $\chi^2(16) = 309.71$; $p < 0.0001$).

Data are presented as mean ± SEM. Solid and empty circles (in C and E) represent animal averages and all images quantified, respectively. Significance was tested using linear mixed effects models with post-hoc pairwise comparisons.

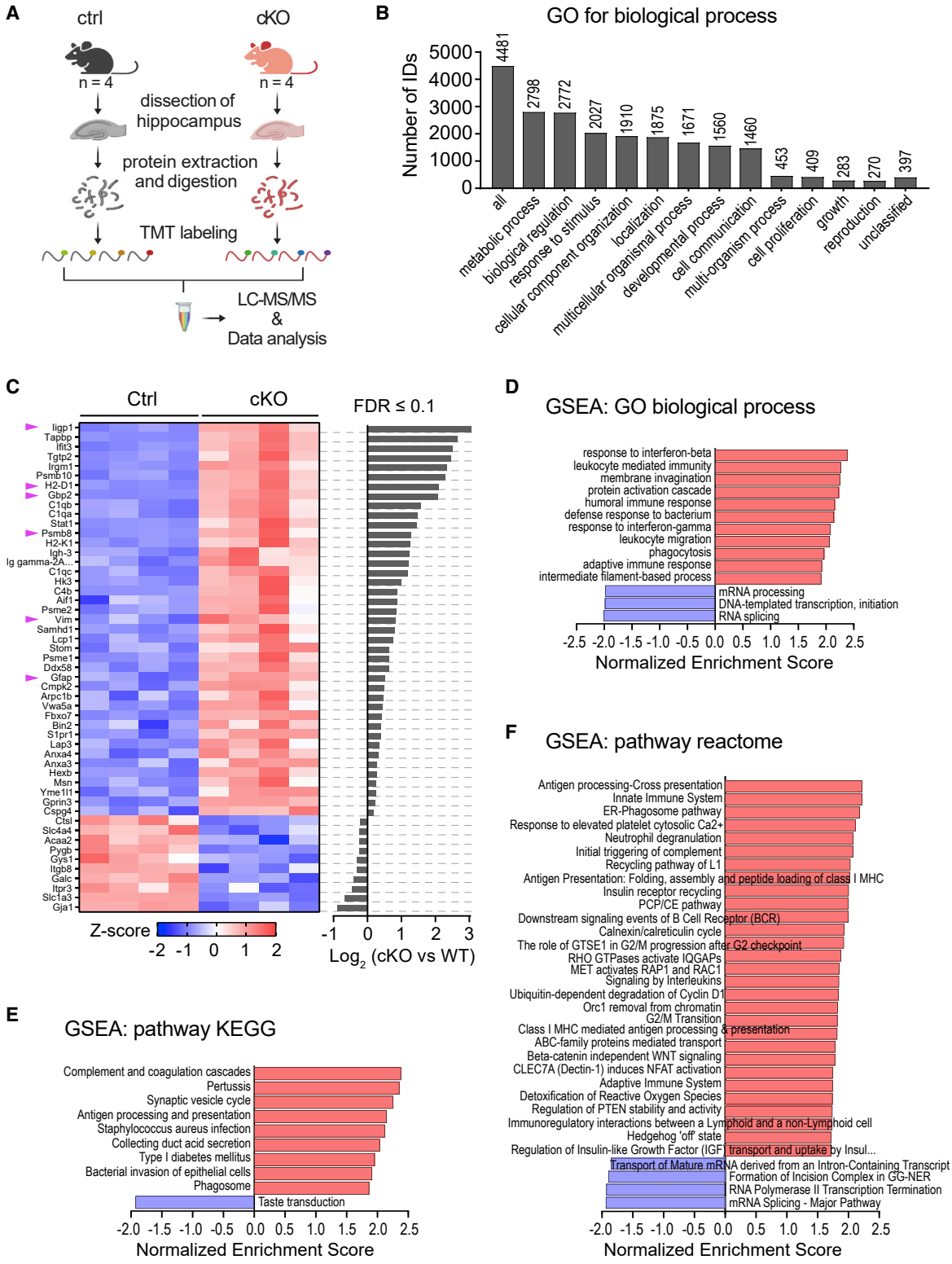

Figure 3. TMT-based proteomics analysis of hippocampal lysates

(A) Hippocampi were dissected from ctrl and cKO mice around 120 dpi. Extracted and digested proteins from n = 4 biological replicates were labeled with tandem mass tags (TMTs) and then pooled for liquid chromatography-tandem mass spectrometry (LC-MS/MS). Scheme created with BioRender.

(legend continued on next page)

We wondered whether the decrease in basal excitability is accompanied by changes in glutamatergic neurotransmission. We first examined AMPA receptor (AMPAR)-mediated miniature excitatory postsynaptic currents (mEPSCs) and found a significant increase in event frequency (Figure 5A) and amplitudes (Figures 5B and 5C), indicating an enhanced synaptic excitatory transmission in cKO mice. Since synaptic density was unchanged in cKO mice (Figure S6E), the increase in mEPSC frequency may result from changes in synaptic release probability. However, excitatory paired-pulse facilitation of Schaffer collateral synapses was unchanged (Figure 5D), indicating that presynaptic glutamate release was not affected. To determine whether postsynaptic changes contributed to the enhanced synaptic excitatory transmission, we examined the AMPAR and NMDA receptor (NMDAR) components of evoked EPSCs and found an elevated AMPA/NMDA ratio by 70% ± 26% ($p = 0.0162$) in cKO mice (Figure 5E).

Changes in glutamate clearance efficacy could influence excitatory synaptic strength (Pannasch et al., 2014). Developmental deletion of Cx30 and Cx43 was reported to reduce astroglial glutamate clearance, affecting NMDAR current kinetics (Pannasch et al., 2011). To determine whether adult cKO mice may likewise show impaired glutamate clearance, we investigated the decay kinetics of evoked NMDAR EPSCs at different stimulation frequencies. At single pulse, 50-Hz, or 100-Hz stimulations, we observed no difference in the decay kinetics of NMDAR currents between genotypes (Figure 5F), suggesting that glutamate uptake was not altered. Synaptic stimulation at 50 Hz prolonged NMDAR EPSCs compared with single pulses (Figure 5F), likely due to slower astrocytic glutamate uptake during high-frequency synaptic activity (Romanos et al., 2019). Interestingly, NMDAR current decay kinetics were significantly faster at 100 Hz compared with 50 Hz ($p = 0.046$ in controls and $p = 0.012$ cKO mice; paired t test), similar to what has been described for pyramidal neurons in the anterior cingulate cortex (Romanos et al., 2019). This suggests that the high-frequency-induced increase in glutamate uptake capacity also occurs at CA1 synapses and is unchanged in cKO mice (Figure 5F).

Thus, it is reasonable to infer that postsynaptic AMPAR density must be elevated in cKO mice, given that both AMPAR mEPSC amplitudes and AMPA/NMDA ratio were increased without overt alterations in presynaptic glutamate release and perisynaptic glutamate clearance. The increased amplitude and frequency in AMPAR mEPSCs may be due to a homeostatic synaptic scaling and activation of silent synapses (Fernandes and Carvalho, 2016; Liao et al., 2001) in response to the lower CA1 neuronal excitability observed in cKO animals. Of note, such an increase in postsynaptic AMPAR density, higher AMPA/NMDA ratio, and activation of silent synapses in CA1 pyramidal neurons were previously also reported in *Cx30*$^{-/-}$*:Cx43*$^{fl/fl}$*:hGFAP-Cre* mice (Pannasch et al., 2011).

Given the homeostatic changes in neuronal excitability and synaptic transmission, we wondered whether synaptic plasticity was also affected in cKO mice. We examined long-term potentiation (LTP) by recording field potentials induced by theta-burst stimulation (three 2-s trains of 100 Hz, 20 s apart) of Schaffer collaterals. Indeed, we found a decreased LTP induction in cKO mice (Figure 5G). Lower LTP induction might be due to a ceiling effect caused by an already higher AMPAR-mediated synaptic strength (Li et al., 2016). However, other processes affecting synaptic potentiation may also be involved. D-serine is the endogenous co-agonist of NMDARs, and the release of D-serine from astrocytes regulates hippocampal LTP (Adamsky et al., 2018; Henneberger et al., 2010; Papouin et al., 2017). We therefore examined whether D-serine availability at CA1 synapses was altered. To address this, we recorded NMDAR-mediated fEPSPs before and after application of saturating concentrations (50 μM) of exogenous D-serine (Figures 5H and S9). Strikingly, we found that the extent of NMDAR-fEPSP potentiation by D-serine was reduced. In control mice, the NMDAR fEPSP slopes increased by 42% ± 7%, whereas in cKO mice, the NMDAR response was only potentiated by 15% ± 5% ($p = 0.0170$; Figures 5H and S9). This finding may indicate a higher ambient level of D-serine in the CA1 of cKO mice (Papouin et al., 2017). Interestingly, a high level of extracellular D-serine was shown to perturb astrocyte-mediated synaptic potentiation in the hippocampus (Adamsky et al., 2018). And D-serine availability controls NMDAR activation during synaptic transmission and impacts learning and memory (Papouin et al., 2017).

Taken together, CA1 neuronal excitability and excitatory synaptic transmission were altered in cKO mice. Also, hippocampal LTP was occluded, which may be due to changes in D-serine homeostasis and saturation of synaptic plasticity.

Spatial learning and memory are impaired in cKO mice

Alterations in CA1 synaptic plasticity may cause deficits in cognitive functions. Before inspecting hippocampus-dependent working memory, we first assessed overall sensorimotor performance. We tested cKO mice and littermate controls before tamoxifen treatment and then at 30, 60, and 90 dpi, using behavioral paradigms that included gait analysis, ledge test, hindlimb clasping, and horizontal wire assays (Figure S10A). As expected, both groups of mice showed a similar score before tamoxifen treatment (pretam). However, starting from 30 to 60 dpi, cKO mice developed subtle sensorimotor deficits that became more pronounced at 90 dpi ($p = 0.0001$; Figure S10A). We then

(B) Of the 4,841 detected proteins (see also Table S1), 4,481 proteins were unambiguously mapped to 4,480 unique entrezgene IDs. Bar chart shows the gene ontology (GO) annotation and functional classification of identified proteins using GO term biological process. GO summary was obtained via WebGestalt.org (Liao et al., 2019).

(C) Heatmap showing relative upregulation (red) or downregulation (blue) of 51 proteins (depicted are gene names) with a false discovery rate (FDR) ≤ 0.1 and ranked by $\log_2$ fold changes between cKO and ctrl mice (right bar graph). Arrowheads indicate proteins (i.e., Iigp1, H2-D1, Gbp2, Psmb8, GFAP, and Vim) known to be upregulated in astrocytes upon microglial cytokine-mediated inflammation (Liddelow et al., 2017). Note the Cx43 (Gja1) reduction in cKO mice (FDR = 0.003); however, Cx30 (Gjb6) was not detected in our proteome. Row *Z* scores were calculated using normalized protein intensities. WT, wild type.

(D–F) Gene enrichment analyses (GSEAs) for categories (D) GO biological process, (E) pathway KEGG, and (F) pathway Reactome with a significance level FDR < 0.05. GSEA analysis was done with WebGestalt.org using all identified proteins ranked by $\log_2$ fold changes between cKO and ctrl mice as input list. Note the overall increased pro-inflammatory signature in cKO hippocampal lysates. GTPase, guanosine triphosphatase; MHC, major histocompatibility complex.

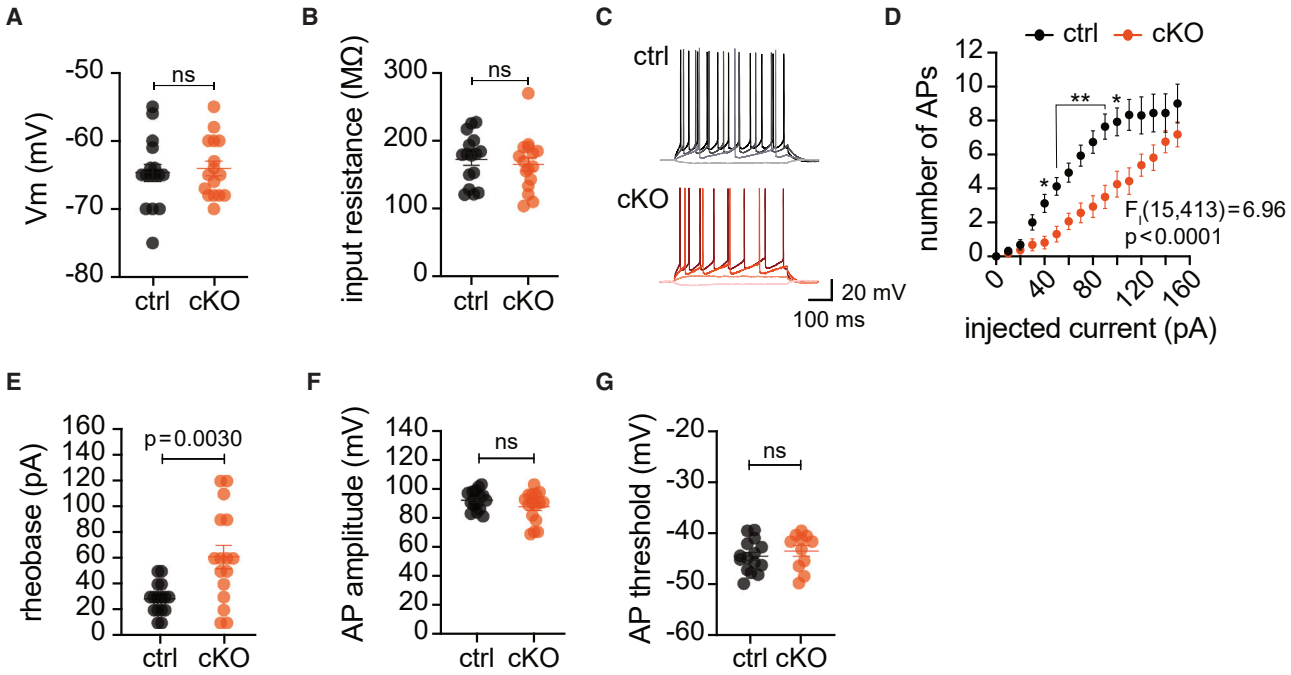

Figure 4. Reduced excitability in CA1 pyramidal cells from cKO mice

(A and B) Resting membrane potential, V_m (A), and input resistance (B) in CA1 pyramidal cells were similar in ctrl (n = 16 cells) and cKO mice (n = 16 cells). (A) Average V_m of ctrl = −64.7 ± 1.3 mV and of cKO = −64.1 ± 1.1 mV is shown (t(30) = 0.37; p = 0.7127; unpaired t test). (B) Average input resistance of ctrl = 172.4 ± 9.1 MΩ and of cKO = 165.1 ± 10.1 MΩ is shown (t(30) = 0.54; p = 0.5937; unpaired t test).

(C) Representative traces of CA1 pyramidal cell firing action potentials (APs) from ctrl and cKO mice. Responses to −20, +30, +80, and +130 pA current injections for 500 ms are shown.

(D) Reduced AP firing in pyramidal cells from cKO mice (n = 16 cells) compared with ctrl (n = 16 cells; $F_{interaction}(15, 413) = 6.96$; $p < 0.0001$; mixed-effects analysis with Sidak's multiple comparisons test: *$p < 0.05$ and **$p < 0.01$).

(E) Reduced AP firing in cKO mice resulted from a higher rheobase compared with ctrl (t(18.3) = 3.41; p = 0.003; Welch's t test).

(F and G) AP amplitude (F) and AP threshold (G) were unchanged in pyramidal cells from cKO mice. AP thresholds were obtained from +80 pA current injections. Data are presented as mean ± SEM.

examined whether cKO mice develop deficits in learning and memory. For this, we tested for object recognition memory (Figure S10B) and for spatial reference learning and memory (Figure 6). Importantly, for each behavioral paradigm, the same group of animals was tested before tamoxifen treatment and then later at 90 dpi; hence, cKO animals at pretam also served as their own controls. We tested the ability of cKO animals to recognize and remember familiar objects using the novel object recognition test (Goulart et al., 2010; Leger et al., 2013) at retention intervals of 3 h and 24 h. Neither short-term nor long-term recognition memory was impaired in cKO mice (Figure S10B). Of note, since novel objects replaced the familiar object at the same location in the box, the novel object recognition test did not require spatial working memory. To directly assess spatial memory, which is primarily controlled by the hippocampus (Broadbent et al., 2004; Moser et al., 1998), we performed a Barnes maze test (Figure 6A). Before tamoxifen treatment, both groups of mice showed similar learning abilities to locate the target hole during the acquisition phase (Figure 6B) and performed equally well during memory recall (Figures 6D and 6E). However, at 90 dpi, cKO mice revealed a significant deficit in spatial learning (Figure 6C) and a complete lack of memory for target location (Figures 6G and 6H). Importantly, memory performance was not influenced by possible changes in motivation or locomotor activity since walking distance during the defined test period was identical between the genotypes (Figures 6F and 6I).

In summary, decoupling astrocytes in adult mice alters hippocampal synaptic transmission and long-term plasticity, which is followed by a pronounced impairment in spatial reference learning and memory.

Calcium signaling and microdomain properties are altered in cortical astrocytes of cKO mice

By facilitating the release and/or uptake of neuroactive molecules, calcium signaling in astrocytes can influence neuronal excitability, synaptic plasticity, and neural circuits controlling behavior (Adamsky et al., 2018; Nagai et al., 2021; Semyanov et al., 2020; Yu et al., 2018). We therefore investigated whether astrocytic calcium dynamics were altered in cKO mice. We performed *in vivo* two-photon imaging of cortical astrocytes expressing the genetically encoded calcium sensor GCaMP6f (Chen et al., 2013) by adeno-associated virus (AAV) delivery using AAV-9/2-hGFAP-GCaMP6f (Figure 7A). Mice were trained for head-restrained, awake imaging as previously described (Glück et al., 2021; Zuend et al., 2020). Astrocytic calcium signals were analyzed using semi-automated image processing and an

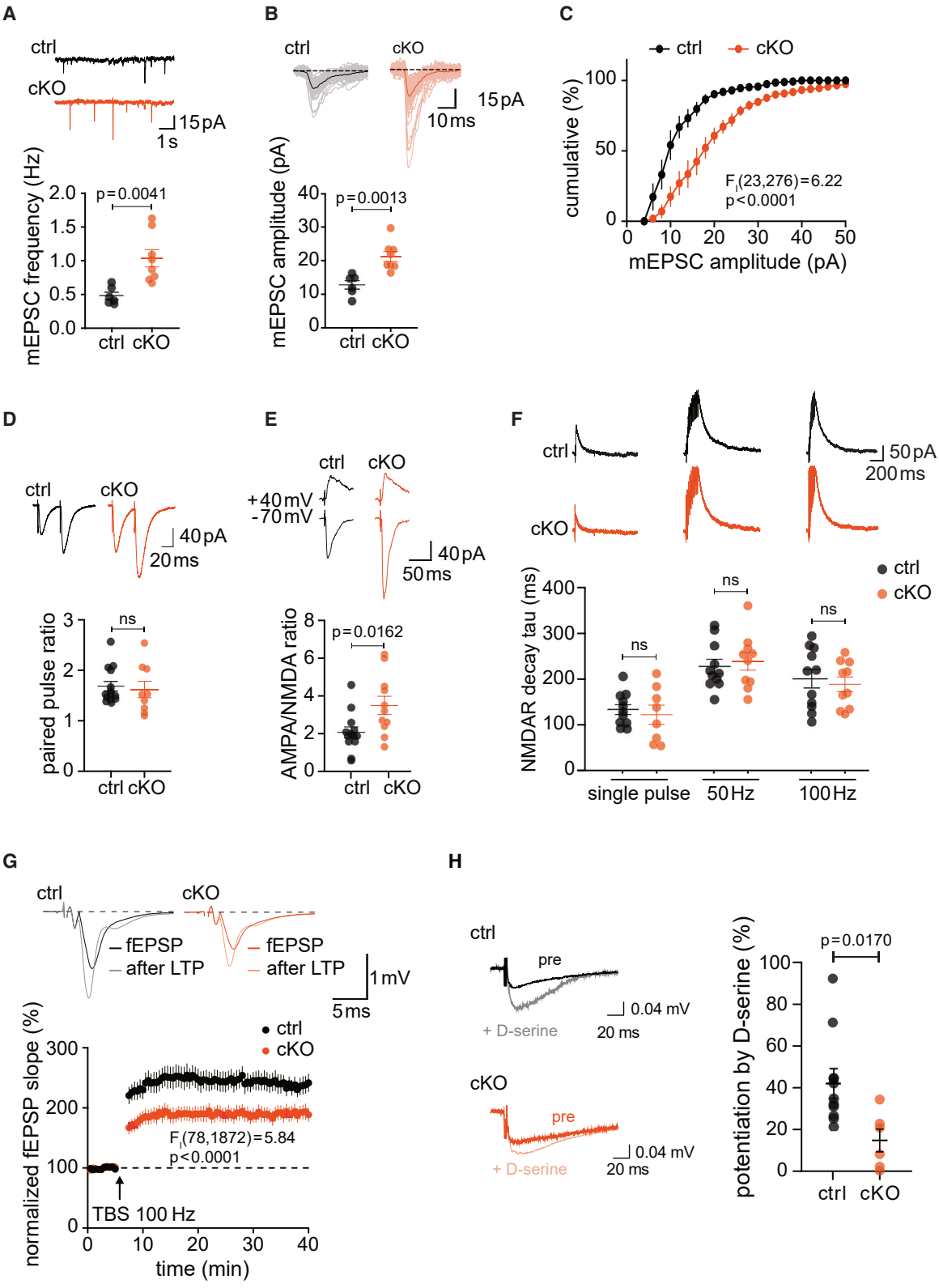

(legend on next page)

activity-based algorithm (Barrett et al., 2018) to identify active regions in imaged fields of view, as employed in earlier studies (Glück et al., 2021; Stobart et al., 2018a; Zuend et al., 2020). We examined calcium signals from astrocytic somas and processes (Figure 7A) and assessed frequency, amplitude, and duration (half-width) of detected calcium transients (Figures 7B–7D). Calcium signal frequency in somas and processes were similar between the genotypes (Figure 7B). However, signal amplitudes were significantly larger in both somas (by ~2.7-fold; $p < 0.001$) and processes (by ~1.3-fold; $p < 0.001$; Figure 7C). We also found adaptations in the duration of astrocytic calcium signals, with shorter signal durations in astrocytic somas from cKO mice (7.6 ± 0.3 s) compared with controls (8.4 ± 0.3 s; $p = 0.0104$; Figure 7D) and slightly longer signal durations in astrocytic processes from cKO mice (7.0 ± 0.1 s) compared with controls (6.7 ± 0.1 s; $p = 0.0032$; Figure 7D). We also assessed the properties of active microdomains in astrocytic processes (automatic activity-based detection) and found that the average number of active domains per astrocyte did not differ between the genotypes (Figure 7E); however, the average size of active domains was 27.5% ± 8.6% ($p < 0.001$) larger in cKO mice (Figure 7F). Thus, we determined that alterations in astrocytic calcium activity and microdomain properties are an additional consequence of reducing astrocytic connexins and network coupling in adult mice, which may contribute to the cellular and behavioral phenotype observed in cKO mice.

DISCUSSION

Astrocytes are involved in a wide range of brain functions across many brain regions (Adamsky et al., 2018; Clasadonte et al., 2017; Nagai et al., 2019; Saab et al., 2012; Suzuki et al., 2011; Yu et al., 2018). They form large intercellular networks as they are coupled by gap junction channels, mainly comprising Cx30 and Cx43 connexin proteins (Giaume et al., 2010; Griemsmann et al., 2015). However, in the adult brain, the functional relevance of the astroglial network *in vivo* remains poorly understood. In this study, we addressed the importance of astrocyte coupling for neural integrity, hippocampal physiology, and behavior in adult mice by selectively deleting Cx30 and Cx43 from astrocytes in a tamoxifen-inducible manner. We revealed that disrupting the astroglial network induces glial activation, alters hippocampal CA1 neuron excitability and synaptic transmission, and impairs long-term synaptic plasticity. This was accompanied by sensorimotor deficits and an impairment in hippocampus-dependent spatial learning and memory. Our results demonstrate the vital contribution of an intact astroglial network in maintaining glial and neuronal homeostasis and its impact on cognitive functions in the adult brain.

Astroglial coupling in the hippocampus was reduced by around 75% in cKO mice. Since astrocytic coupling is completely lost in mice with a total deletion of Cx30 and Cx43 (Pannasch et al., 2011; Wallraff et al., 2006), the residual coupling in cKO mice reflects an incomplete Cre recombination using the GLAST-CreERT2 driver line (Jahn et al., 2018; Mori et al., 2006). Indeed, immunohistochemistry revealed single astrocytes still expressing Cx30 and Cx43 in cKO brain sections at 90 dpi. Nevertheless, an ~90% and ~60% reduction in Cx30 and Cx43 expression, respectively, was achieved in both cortex and hippocampus. The different extent of Cx30 and Cx43 protein depletion could be explained by potential differences in recombination efficiency between the two floxed alleles. Another possibility is that Cx43, unlike Cx30, may not be exclusively expressed by astrocytes (Reichenbach et al., 2019; Rouach et al., 2002), which could lead to an underestimation of astrocytic Cx43 depletion.

Mice with developmental ablation of Cx30 and Cx43 were reported to develop early-onset gray and white matter pathology that comprises vacuolation, dysmyelination, and axonal degeneration (Lutz et al., 2009). In these mice, tissue damage was associated with astrogliosis, but microglial activation was absent (Lutz et al., 2009). In our study, disrupting astrocytic coupling in the adult brain initiated a widespread astrocyte and microglia activation but in the absence of visible tissue damage or neural degeneration. We found upregulation of astrocytic markers associated with neuroinflammation-induced astrocytic reactivity (Diaz-Castro et al., 2021; Liddelow et al., 2017). We also detected changes in microglial markers ($CLEC7A^{high}$ and $P2YR12^{low}$) that are

Figure 5. Alterations in hippocampal excitatory synaptic transmission and plasticity in cKO mice

(A–C) AMPAR-mediated mEPSC (recorded at −70 mV in the presence of 1 μM TTX and 25 μM bicuculline-methiodide) frequency (A) and amplitudes (B and C) were increased in CA1 pyramidal cells from cKO mice. Upper panel in (A) shows sample mEPSC traces from ctrl (n = 6 cells) and cKO (n = 8 cells) recordings. mEPSC frequency was increased by 0.56 ± 0.16 Hz compared with ctrl ($t(12) = 3.54$; $p = 0.0041$; unpaired t test). (B) mEPSC amplitudes were increased by 8.5 ± 2.0 pA in cKO mice compared with ctrl ($t(12) = 4.16$; $p = 0.0013$; unpaired t test). (C) Cumulative distribution of mEPSC amplitudes differed between genotypes ($F_{interaction}(23,276) = 6.215$; $p < 0.0001$; two-way ANOVA).

(D) Paired pulse ratio was not altered in cKO mice (n = 9 cells) compared with ctrl (n = 14 cells; $U = 50.50$; $p = 0.4479$; Mann-Whitney U test). Sample EPSC traces (50-ms interstimulus interval) are shown above the graph.

(E) AMPA/NMDA EPSC ratio was increased in cKO mice (n = 11 cells) compared with ctrl (n = 13 cells; $t(22) = 2.61$; $p = 0.0162$; unpaired t test), likely due to increased AMPAR activity in cKO mice. Representative NMDAR and AMPAR EPSC traces are shown above the graph.

(F) Decay kinetics of NMDAR EPSCs evoked with a single pulse stimulation or with 10 pulses at 50 Hz and 100 Hz were similar in ctrl (n = 8–10 cells) and cKO mice (n = 11 cells; single pulse: $t(17) = 0.55$, $p = 0.5868$; 50 Hz: $t(19) = 0.43$, $p = 0.6753$; and 100 Hz: $t(19) = 0.49$, $p = 0.6271$; unpaired t tests). In both genotypes, decay kinetics increased from single-pulse to 50-Hz stimulations (ctrl: $t(10) = 5.80$, $p = 0.0002$; cKO: $t(7) = 3.70$, $p = 0.0081$; paired t test) and decreased from 50 Hz to 100 Hz stimulation (ctrl: $t(10) = 2.27$, $p = 0.0463$; cKO: $t(9) = 3.20$, $p = 0.0117$; paired t test).

(G) Theta-burst stimulation (TBS)-induced LTP (arrow, three 2-s trains of 100 Hz, 20 s apart) was reduced in cKO mice (n = 14 slices) compared with ctrl (n = 12 slices; $F_{interaction}(78, 1,872) = 5.84$, $p < 0.0001$, two-way ANOVA; comparison 32–42 min after TBS: $t(24) = 2.7$, $p = 0.0125$, unpaired t test). Sample traces represent averaged fEPSPs before and 40 min after TBS.

(H) Example of NMDAR-mediated fEPSP traces (left panel) from ctrl and cKO recordings before and after addition of 50 μM D-serine. Reduced potentiation by D-Serine in cKO mice (n = 6) compared with ctrl is shown (n = 10; $t(14) = 2.71$; $p = 0.0170$; unpaired t test).

Data are presented as mean ± SEM.

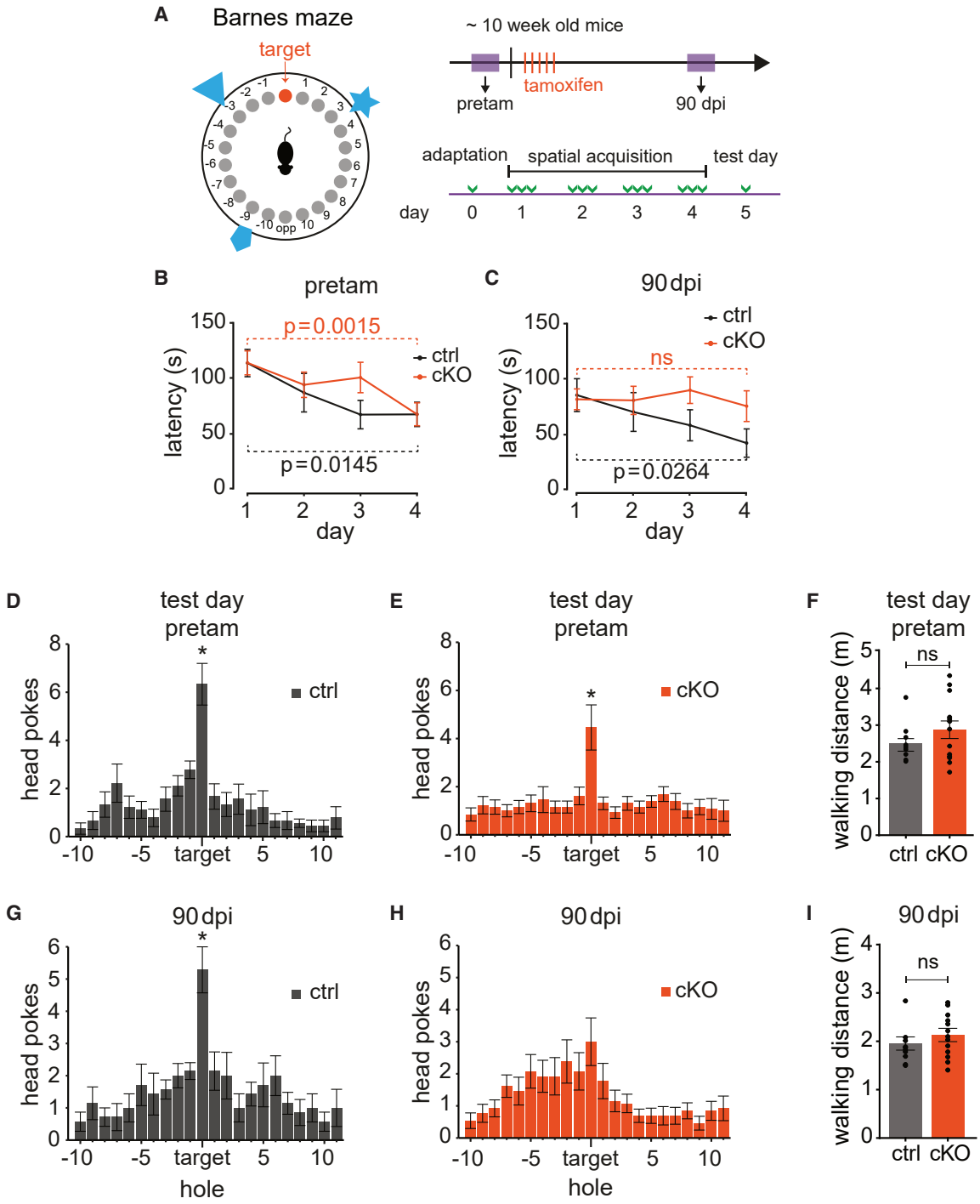

Figure 6. Impaired spatial learning and memory in cKO mice

(A) Left: scheme of Barnes maze table with 22 holes, with one escape hole (target) and spatial cues (blue symbols). Right: experimental procedure to test spatial learning (4 days acquisition phase) and memory retrieval (test day 5, with target hole sealed) in adult mice before tamoxifen treatment (pretam) and at 90 dpi is shown. Green arrowheads indicate sessions.

(B and C) Assessment of spatial learning, latency (s) to find target hole, at pretam (B) and at 90 dpi (C). At pretam, ctrl (n = 9) and cKO mice (n = 13) learned equally well with a significant drop in latencies from day 1 to 4 (ctrl: $\beta = 41.76$, $t(56.2) = 2.52$, $p = 0.0145$; cKO: $\beta = 45.94$, $t(56.2) = 3.34$, $p = 0.0015$). However, at 90 dpi, only ctrl mice showed a significant learning effect by day 4 (ctrl: $\beta = 42.77$, $t(56.2) = 2.28$, $p = 0.0264$; cKO: $\beta = 6.11$, $t(56.2) = 0.44$, $p = 0.6589$).

(legend continued on next page)

characteristic for DAM, which are described to be more phagocytic and often reported in the vicinity of degenerating neurons and myelin debris (Butovsky and Weiner, 2018; Hickman et al., 2013; Keren-Shaul et al., 2017; Krasemann et al., 2017). Despite no visible neural, synaptic, or myelin loss, we cannot rule out that microglia and/or astrocytes have increased phagocytic activity in cKO mice. Importantly, our findings highlight that, in adulthood, an intact glial network and astrocytic connexins may be critical for the physiological interaction between astrocytes and microglia. Indeed, a complex dialogue between microglia and astrocytes is known to shape tissue homeostasis and cellular functions in CNS health and disease (Liddelow et al., 2020; Vainchtein and Molofsky, 2020), and their cross talk can engender both neuroprotective or detrimental effects (Aguzzi et al., 2013; Liddelow et al., 2017; Rothhammer et al., 2018). However, most research on microglia-astrocyte interactions is done in the context of injury, trauma, or degenerative diseases. And very little is known about the physiological interactions of these cells. Hence, future studies with our inducible mouse model could further address how microglial behavior is altered upon decoupling astrocytes, which could provide novel insights into the intercellular dynamics of these cells.

Since overall brain myelination and myelin integrity was preserved in adult cKO mice, we can safely conclude that the previously reported deficits are primarily caused by a developmental disruption of the glial network, before and during the peak phase of CNS myelination (Lutz et al., 2009). Oligodendrocytes are coupled to astrocytes by gap junction channels, forming a panglial syncytium that is suggested to maintain potassium siphoning (Menichella et al., 2006; Orthmann-Murphy et al., 2007; Rash, 2010) as well as the supply of metabolites between capillaries and axonal compartments (Meyer et al., 2018; Morrison et al., 2013; Saab et al., 2013). However, it is still unclear whether panglial coupling is required for adult myelin maintenance and axonal integrity. Our study suggests that panglial coupling is not critical for adult myelin maintenance and axonal health, at least in the absence of specific challenges. Alternatively, the residual panglial syncytium in cKO mice might be sufficient to maintain myelin and axonal integrity. The extent to which intercellular coupling is reduced in white matter tracts of cKO animals remains to be determined, and follow-up studies could further resolve whether alterations in panglial coupling impact axonal physiology and energy homeostasis (Looser et al., 2018; Saab et al., 2016).

Our results from hippocampal electrophysiological recordings are in part consistent with prior findings in postnatal recordings from *Cx30*$^{-/-}$*:Cx43*$^{fl/fl}$*:hGFAP-Cre* mice, which were reported to have enhanced excitatory synaptic transmission and altered postsynaptic properties at CA1 synapses (Pannasch et al., 2011). However, we observed a significant reduction in the excitability of CA1 pyramidal cells in adult cKO mice, in contrast to the increased excitability observed in developing knockouts (Pannasch et al., 2011). Contrary to our study, Pannasch et al. (2011) performed their measurements in the presence of picrotoxin to block inhibitory input, while we measured cellular excitability in the absence of synaptic blockers. Hence, inhibitory input may also be enhanced in CA1 pyramidal cells in adult cKO mice, similar to that previously reported (Pannasch et al., 2011). Indeed, an increase in inhibitory input and shunting conductance could shift the stimulus intensity required to generate action potentials in CA1 pyramidal neurons (Bonin et al., 2007; Pavlov et al., 2009). Of note, astrocytes are known to regulate extracellular γ-aminobutyric acid (GABA) homeostasis and tonic inhibition of neurons (Mederos and Perea, 2019; Yu et al., 2018). However, whether inhibitory conductance is elevated in CA1 neurons following astrocytic decoupling remains to be determined. What appears at odds is the reduction in basal synaptic transmission (extracellularly recorded without synaptic blockers) while excitatory synaptic transmission (intracellularly recorded in the presence of bicuculline) is enhanced in cKO mice. Evoked extracellular field responses in stratum radiatum are generated from a population of neuronal dendrites that are influenced by feedforward inhibition via GABAergic neuron activation (Alger and Nicoll, 1982; Buzsáki, 1984), which may be augmented in cKO mice. Indeed, addition of the $GABA_A$ channel blocker picrotoxin enhances hippocampal fEPSPs (Buzsáki, 1984; Ko et al., 2014). Nonetheless, further investigation is needed to show how the inhibition-excitation balance is altered following astrocyte decoupling in adult mice.

In CA1 neurons, we found an increase in the frequency of AMPAR-mediated mEPSCs that could not be explained by changes in presynaptic glutamate release or synaptic density. Of note, paired-pulse responses were recorded from activated Schaffer collaterals that project mostly to the stratum radiatum, where synaptic density was also determined in cKO animals. However, CA1 neurons also receive excitatory synapses in the stratum lacunosum moleculare (e.g., from entorhinal cortex afferents), which may have altered properties or density in cKO mice that could explain the increase in mEPSC frequency. Another possibility is that the numbers of silent synapses could be reduced in adult cKO mice, similar to what has been observed in postnatal *Cx30*$^{-/-}$*:Cx43*$^{fl/fl}$*:hGFAP-Cre* mice (Pannasch et al., 2011). In addition, in line with previous findings (Pannasch et al., 2011), we detected an increase in excitatory synaptic transmission that is likely mediated by an increase in postsynaptic AMPAR density, given that presynaptic glutamate release and glutamate clearance were not overtly perturbed in cKO mice. Overall, these synaptic changes could reflect a homeostatic scaling up of

(D and E) At pretam, both genotypes had a similar spatial memory performance. Bar graphs represent number of head pokes into each hole during a 90-s session on test day 5. Ctrl (n = 9) and cKO mice (n = 13) clearly distinguished the target hole (ctrl: comparison to hole −1, $\beta = -3.56$, $Z = -5.60$, $p < 0.0001$; cKO: comparison to hole −1, $\beta = -3.56$, $Z = -6.28$, $p < 0.0001$).

(F) No difference in walking performance on test day 5 between genotypes at pretam (n = 9–13; $t(20) = -1.07$; $p = 0.2096$; unpaired t test).

(G and H) At 90 dpi, only ctrl mice (G), but not cKO mice (H), were able to distinguish the target hole on test day 5 (ctrl: comparison to hole −1: $\beta = -3.29$, $Z = -5.55$, $p < 0.0001$; cKO: comparison to hole −7: $\beta = -1.38$, $Z = -2.51$, $p = 0.1414$).

(I) No difference in walking performance on test day 5 between genotypes at 90 dpi (n = 9–13; $t(20) = -0.96$; $p = 0.3470$; unpaired t test).

Data are mean ± SEM. Significance was tested with linear mixed effects models and post-hoc pairwise comparisons (in B and C) or Dunnett's post-hoc tests (in D, E, G, and H).

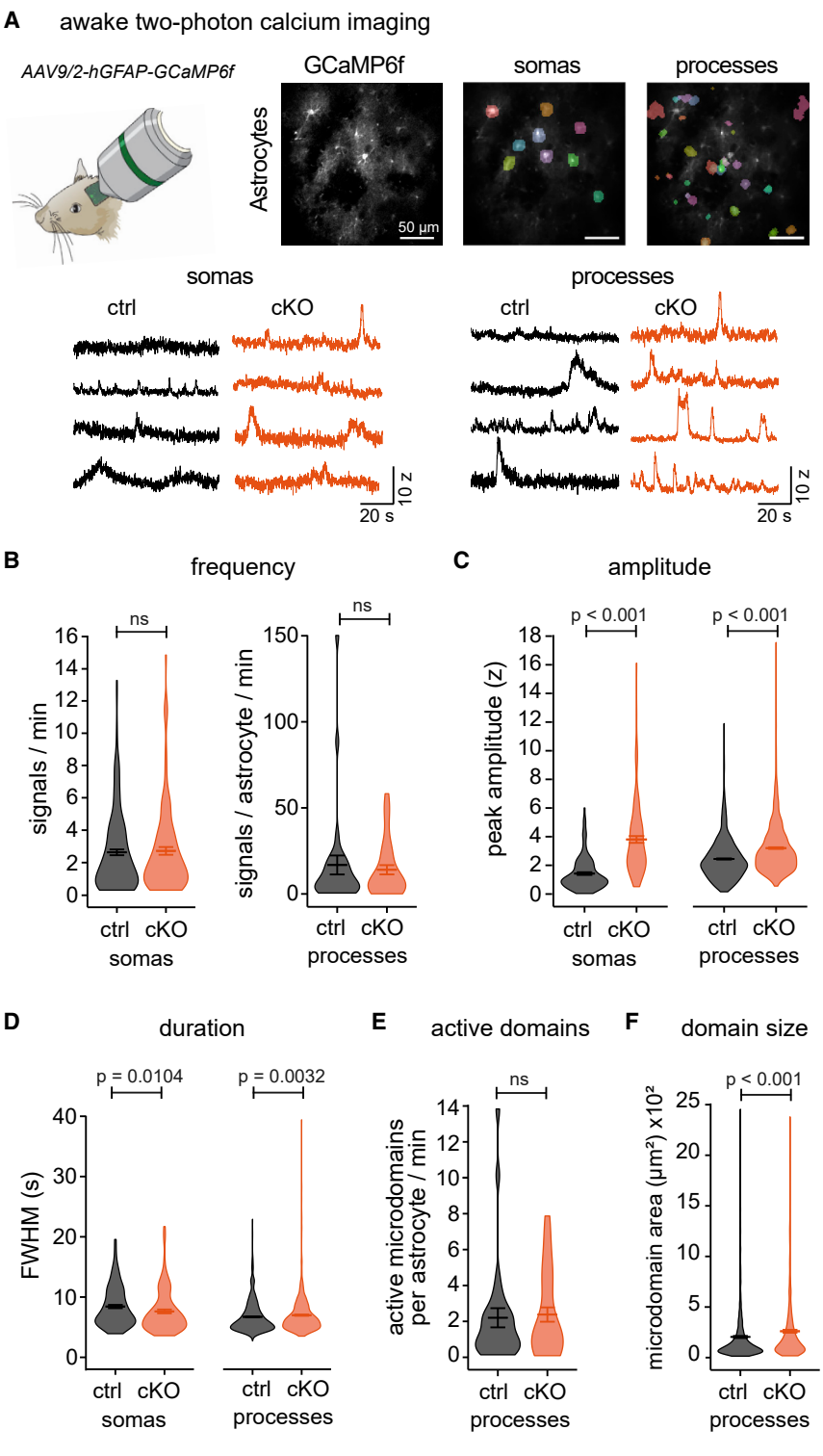

Figure 7. Altered astrocytic calcium signaling in cKO mice *in vivo*

(A) Awake two-photon calcium imaging in cortical astrocytes expressing GCaMP6f (via AAV9/2-hGFAP-GCaMP6f delivery into somatosensory cortex). Example image of astrocytes *in vivo* (left panel) and example regions of interest (ROIs) for somas (determined by hand) and processes (determined by activity-based algorithm) are shown. Lower panels show normalized (*Z*-scored) calcium traces from astrocytic somas and processes from ctrl (black) and cKO mice (red). Calcium imaging was performed around 90 dpi.

(B) Frequency of calcium signals in somas and processes were comparable between the genotypes. Average signals/min in somas of ctrl = 2.70 ± 0.18 and of cKO = 2.79 ± 0.24 ($p = 0.763$) and average signals/astrocyte/min in processes of ctrl = 16.8 ± 5.5 and of cKO = 14.0 ± 2.7 ($p = 0.974$) are shown.

(C) Peak amplitudes (*Z*-scored) of calcium transients were larger in astrocytic somas and processes of cKO mice compared with ctrl. Average amplitude (SD) in somas of ctrl = 1.41 ± 0.10 and of cKO = 3.81 ± 0.24 ($p < 0.001$) and amplitudes in processes of ctrl = 2.45 ± 0.04 and of cKO = 3.21 ± 0.06 ($p < 0.001$) are shown.

(D) Duration (half-width in s) of calcium transients was shorter in somas of cKO mice compared with ctrl (7.6 ± 0.3 s in cKO versus 8.4 ± 0.3 in ctrl; $p = 0.0104$) and slightly longer in processes compared with ctrl (7.0 ± 0.1 s in cKO versus 6.7 ± 0.1 s in ctrl; $p = 0.0032$).

(E) Number of active microdomains per astrocyte per min (determined in processes via activity-based algorithm) was comparable between the genotypes (2.38 ± 0.40 in cKO versus 2.2 ± 0.53 in ctrl; $p = 0.779$).

(F) Size of active domains was larger in cKO mice compared with ctrl (260 ± 15 μm^2 in cKO versus 204 ± 11 μm^2 in ctrl; $p < 0.001$). Data are presented as violin plots with the mean ± SEM.

Data were collected from a total of 187 and 123 astrocytes from 30 to 35 fields of view and imaging sessions from each two ctrl and cKO mice, respectively. Significance was tested with Mann-Whitney U tests.

excitatory synapses in response to the reduced excitability of CA1 neurons (Fernandes and Carvalho, 2016; Liao et al., 2001).

We could demonstrate that hippocampal LTP as well as spatial learning and memory were impaired in adult cKO mice. These impairments could be explained by the observed perturbations in D-serine homeostasis. Astrocytic D-serine release is reported to regulate hippocampal LTP and memory formation (Adamsky et al., 2018; Henneberger et al., 2010; Papouin et al., 2017). Our findings suggest that extracellular D-serine levels are elevated in cKO mice, which may cause a saturation of NMDAR-mediated synaptic potentiation. Indeed, high extracellular D-serine levels impair astrocytic D-serine-induced synaptic potentiation (Adamsky et al., 2018). Elevated extracellular D-serine concentrations could result from changes in neuromodulatory signaling (Papouin et al., 2017), an increase in glycolytic production of L-serine (Le Douce et al., 2020),

calcium-mediated changes in constitutive release from astrocytes (Shigetomi et al., 2013), or deficits in D-serine clearance (Ribeiro et al., 2002). While it still remains to be determined how D-serine homeostasis is altered, we found that astrocyte calcium signaling is elevated in cKO mice, which may influence astrocytic D-serine release (Shigetomi et al., 2013).

The reduced LTP in cKO mice could also be explained by a saturation of synaptic plasticity caused by an already higher AMPAR-mediated synaptic strength (Li et al., 2016). Moreover, synaptic strength can be regulated by glial tumor necrosis factor alpha (TNF-α) (Beattie et al., 2002; Stellwagen and Malenka, 2006) that has been shown to impact memory via astrocyte signaling (Habbas et al., 2015). Given the glial reactivity as well as the increase in cytokine signaling pathways observed in cKO mice, it may well be that elevated TNF-α signaling is also involved in mediating the homeostatic increase in synaptic activity and could contribute to memory impairments seen in cKO mice.

Astrocytes are known to contribute to spatial and contextual memory formation (Adamsky et al., 2018; Suzuki et al., 2011), which also involves lactate mobilization from glycogen stores and lactate release from astrocytes (Alberini et al., 2018; Duran et al., 2013; Zuend et al., 2020). We demonstrate here that spatial memory formation requires an intact astrocytic network, which has been shown to redistribute metabolic resources (Cooper et al., 2020) and facilitate lactate supply to neurons (Clasadonte et al., 2017; Murphy-Royal et al., 2020; Rouach et al., 2008). Interestingly, our hippocampal proteomics analysis revealed that cKO mice have a reduced abundance of glycogen synthase 1 (GYS1) and glycogen phosphorylase (PYGB), which are crucial for astrocytic glycogen homeostasis and lactate mobilization. Moreover, cKO mice have lower levels of the sodium bicarbonate cotransporter 1 (NBCe1, gene name *Slc4a4*), which is critical in regulating astrocytic glucose metabolism and lactate production (Ruminot et al., 2011, 2019). Hence, it may well be that astrocytic lactate supply to neurons is also perturbed in adult cKO mice, which may be an additional factor impacting synaptic plasticity and cognitive abilities (Alberini et al., 2018; Duran et al., 2013; Suzuki et al., 2011; Zuend et al., 2020). Whether and how glucose and glycogen metabolism are altered upon decoupling astrocytes in adult mice remains to be seen.

The astrocytic network has also been described to play an important role in buffering extracellular potassium released during synaptic activity (Pannasch et al., 2011; Wallraff et al., 2006). Since resting membrane potentials of CA1 pyramidal neurons and astrocytes were unchanged in cKO mice, basal extracellular potassium levels should be normal, as reported earlier (Pannasch et al., 2011). However, we cannot exclude possible deficits in spatial buffering of potassium during elevated neuronal activity in cKO mice. Yet it was recently demonstrated that astrocytic gap junction coupling is not required for buffering potassium transients evoked by synaptic activity in CA1 stratum radiatum (Breithausen et al., 2020). Moreover, in line with previous electroencephalogram (EEG) recordings in *Cx30*$^{-/-}$*:Cx43*$^{fl/fl}$*:hGFAP-Cre* mice (Chever et al., 2016), throughout all our behavioral tests in cKO mice, we never noticed any spontaneous seizures, which might be expected if potassium clearance was severely perturbed (Larson et al., 2018).

Astrocytes normally have a territorial organization and avoid overlap with neighboring astrocytes along their borders (Bushong et al., 2002; Oberheim et al., 2008). Reduction of astrocytic connexins and coupling may have disrupted the astrocytic territorial organization in adult cKO mice, likely because astrocytes appeared to occupy larger territories (revealed by more and longer processes), yet astrocyte density was unchanged. Interestingly, loss of astrocytic domain organization and an increase in overlapping processes between astrocytes are not general features of astrogliosis but occur in certain pathophysiological conditions, such as epilepsy (Oberheim et al., 2008). The functional consequences of an increase in overlapping astrocytic processes are still unclear and difficult to investigate. Yet it is intriguing to speculate that gap junction coupling between connected astrocytes ensures their territorial organization in the adult brain.

Taken together, our findings showcase that astrocytic connexins and an intact glial syncytium are critical for neural homeostasis, information processing, and brain function in adult mice.

Limitations of the study

Our study is mostly descriptive in nature, reporting the cellular and functional alterations as a result of the loss of astrocytic connexins and coupling, but lacks precise mechanisms to explain the results. We found changes in astrocyte and microglia morphology and marker expressions, indicative of glial activation (Escartin et al., 2021; Liddelow et al., 2020). These changes may reflect physiological remodeling accompanied by alterations in various homeostatic functions in both astrocytes and microglia. Hence, it is difficult to determine whether the observed effects in cKO mice are primarily due to insufficient astrocytic network coupling, loss of connexin hemichannel activities, or additional gain (or loss) of functions owing to glial activation. Of note, a recent study revealed that neuronal integrity and synaptic function were not perturbed despite prominent glial activation following bacterial endotoxin lipopolysaccharide-induced neuroinflammation (Diaz-Castro et al., 2021), which cautions that reactive glial transformations do not universally cause neuronal and synaptic dysfunctions. Yet the nature of the glial activation phenotype in cKO mice is not fully resolved. For instance, microglia have been reported to modulate synaptic transmission, and possible changes in microglia-neuron signaling in cKO mice could additionally alter synaptic plasticity and influence learning and memory (Vainchtein and Molofsky, 2020; Wu et al., 2015). We cannot rule out the contribution of Cx43 hemichannel function, which has been implicated in fear-memory consolidation (Stehberg et al., 2012). Besides, channel-independent functions of astrocytic connexins (Pannasch et al., 2014) may also be involved in shaping the phenotype of cKO mice. Thus, given the wide range of functions that connexins may serve beyond intercellular communication, the findings of this study could be influenced by a variety of molecular mechanisms, which require further investigation in the future.

STAR★METHODS

Detailed methods are provided in the online version of this paper and include the following:

SUPPLEMENTAL INFORMATION

Supplemental information can be found online at https://doi.org/10.1016/j.celrep.2022.110484.

ACKNOWLEDGMENTS

We thank Martine Cohen-Salmon for providing Gjb6$^{fl/fl}$ mice; Annika Keller for antibody support and discussion; Michael J. Stobart for technical assistance; Frank Kirchhoff (CIPMM, Homburg) for help in initiating the study; Hanns Ulrich Zeilhofer, Martin Müller, and Mirko Santello for critical input; the Functional Genomics Center Zurich (FGCZ) for proteomics support; members of the Center for Microscopy and Image Analysis of UZH for provision of microscopes and remote access to image analysis tools; the Institute of Epidemiology, Biostatistics and Prevention of UZH for statistical consulting; and Karen Everett for critical reading of the manuscript. A.S.S. received support from a Synapsis Career Fellowship Award, the Neuroscience Center Zurich (ZNZ), the Cloëtta Foundation, and the Swiss National Science Foundation (Eccellenza 187000). B.W. was supported by the Swiss National Science Foundation (SNF no. 31003A_156965).

AUTHOR CONTRIBUTIONS

Conceptualization, L.H., B.W., and A.S.S.; methodology, L.H., N.B., K.D.F., L.T., Z.J.L., M.Z., S.B., M.H., W.M., T.R., and A.S.S.; investigation, L.H., N.B., K.D.F., L.T., Z.J.L., S.B., T.R., H.S.Z., and A.S.S.; resources, K.-A.N., C.G., B.W., and A.S.S.; visualization, L.H. and A.S.S.; writing – original draft, L.H. and A.S.S.; writing – review and editing, L.H., K.D.F., N.B., L.T., Z.J.L., K.-A.N., B.W., and A.S.S.; supervision, A.S.S.; funding acquisition, B.W. and A.S.S.

DECLARATION OF INTERESTS

The authors declare no competing interests.

Received: October 23, 2020
Revised: November 20, 2021
Accepted: February 14, 2022
Published: March 8, 2022

REFERENCES

Adamsky, A., and Goshen, I. (2018). Astrocytes in memory function: pioneering findings and future directions. Neuroscience *370*, 14–26.

Adamsky, A., Kol, A., Kreisel, T., Doron, A., Ozeri-Engelhard, N., Melcer, T., Refaeli, R., Horn, H., Regev, L., Groysman, M., et al. (2018). Astrocytic activation generates de novo neuronal potentiation and memory enhancement. Cell *174*, 59–71.e14.

Aguzzi, A., Barres, B.A., and Bennett, M.L. (2013). Microglia: scapegoat, saboteur, or something else? Science *339*, 156–161.

Alberini, C.M., Cruz, E., Descalzi, G., Bessières, B., and Gao, V. (2018). Astrocyte glycogen and lactate: new insights into learning and memory mechanisms. Glia *66*, 1244–1262.

Alger, B.E., and Nicoll, R.A. (1982). Feed-forward dendritic inhibition in rat hippocampal pyramidal cells studied *in vitro*. J. Physiol. *328*, 105–123.

Araque, A., Parpura, V., Sanzgiri, R.P., and Haydon, P.G. (1999). Tripartite synapses: glia, the unacknowledged partner. Trends Neurosci. *22*, 208–215.

Barrett, M.J.P., Ferrari, K.D., Stobart, J.L., Holub, M., and Weber, B. (2018). CHIPS: an extensible toolbox for cellular and hemodynamic two-photon image analysis. Neuroinformatics *16*, 145–147.

Bates, D., Mächler, M., Bolker, B., and Walker, S. (2015). Fitting linear mixed-effects models using lme4. J. Stat. Softw. *67*, 1–48.

Beattie, E.C., Stellwagen, D., Morishita, W., Bresnahan, J.C., Ha, B.K., Von Zastrow, M., Beattie, M.S., and Malenka, R.C. (2002). Control of synaptic strength by glial TNFalpha. Science *295*, 2282–2285.

Bonin, R.P., Martin, L.J., MacDonald, J.F., and Orser, B.A. (2007). Alpha5GABAA receptors regulate the intrinsic excitability of mouse hippocampal pyramidal neurons. J. Neurophysiol. *98*, 2244–2254.

Boulay, A.-C., del Castillo, F.J., Giraudet, F., Hamard, G., Giaume, C., Petit, C., Avan, P., and Cohen-Salmon, M. (2013). Hearing is normal without connexin30. J. Neurosci. *33*, 430–434.

Breithausen, B., Kautzmann, S., Boehlen, A., Steinhäuser, C., and Henneberger, C. (2020). Limited contribution of astroglial gap junction coupling to buffering of extracellular K+ in CA1 stratum radiatum. Glia *68*, 918–931.

Broadbent, N.J., Squire, L.R., and Clark, R.E. (2004). Spatial memory, recognition memory, and the hippocampus. Proc. Natl. Acad. Sci. U S A *101*, 14515–14520.

Bushong, E.A., Martone, M.E., Jones, Y.Z., and Ellisman, M.H. (2002). Protoplasmic astrocytes in CA1 stratum radiatum occupy separate anatomical domains. J. Neurosci. *22*, 183–192.

Butovsky, O., and Weiner, H.L. (2018). Microglial signatures and their role in health and disease. Nat. Rev. Neurosci. *19*, 622–635.

Buzsáki, G. (1984). Feed-forward inhibition in the hippocampal formation. Prog. Neurobiol. *22*, 131–153.

Cathala, L., Misra, C., and Cull-Candy, S. (2000). Developmental profile of the changing properties of NMDA receptors at cerebellar mossy fiber–granule cell synapses. J. Neurosci. *20*, 5899–5905.

Chao, H., Lin, C., Zuo, Q., Liu, Y., Xiao, M., Xu, X., Li, Z., Bao, Z., Chen, H., You, Y., et al. (2019). Cardiolipin-dependent mitophagy guides outcome after traumatic brain injury. J. Neurosci. *39*, 1930–1943.

Chen, T.-W., Wardill, T.J., Sun, Y., Pulver, S.R., Renninger, S.L., Baohan, A., Schreiter, E.R., Kerr, R.A., Orger, M.B., Jayaraman, V., et al. (2013). Ultrasensitive fluorescent proteins for imaging neuronal activity. Nature *499*, 295–300.

Chever, O., Dossi, E., Pannasch, U., Derangeon, M., and Rouach, N. (2016). Astroglial networks promote neuronal coordination. Sci. Signal. *9*, ra6.

Cina, C., Maass, K., Theis, M., Willecke, K., Bechberger, J.F., and Naus, C.C. (2009). Involvement of the cytoplasmic c-terminal domain of connexin43 in neuronal migration. J. Neurosci. *29*, 2009–2021.

Clarke, L.E., Liddelow, S.A., Chakraborty, C., Münch, A.E., Heiman, M., and Barres, B.A. (2018). Normal aging induces A1-like astrocyte reactivity. Proc. Natl. Acad. Sci. U S A *115*, E1896–E1905.

Clasadonte, J., Scemes, E., Wang, Z., Boison, D., and Haydon, P.G. (2017). Connexin 43-mediated astroglial metabolic networks contribute to the regulation of the sleep-wake cycle. Neuron *95*, 1365–1380.e5.

Cohen-Salmon, M., Regnault, B., Cayet, N., Caille, D., Demuth, K., Hardelin, J.-P.P., Janel, N., Meda, P., and Petit, C. (2007). Connexin30 deficiency

causes instrastrial fluid-blood barrier disruption within the cochlear stria vascularis. Proc. Natl. Acad. Sci. U S A *104*, 6229–6234.

Cooper, M.L., Pasini, S., Lambert, W.S., D'Alessandro, K.B., Yao, V., Risner, M.L., and Calkins, D.J. (2020). Redistribution of metabolic resources through astrocyte networks mitigates neurodegenerative stress. Proc. Natl. Acad. Sci. U S A *117*, 18810–18821.

Diaz-Castro, B., Bernstein, A.M., Coppola, G., Sofroniew, M.V., and Khakh, B.S. (2021). Molecular and functional properties of cortical astrocytes during peripherally induced neuroinflammation. Cell Rep. *36*, 109508.

Le Douce, J., Maugard, M., Veran, J., Matos, M., Jégo, P., Vigneron, P.A., Faivre, E., Toussay, X., Vandenberghe, M., Balbastre, Y., et al. (2020). Impairment of glycolysis-derived L-serine production in astrocytes contributes to cognitive deficits in Alzheimer's disease. Cell Metab. *31*, 503–517.e8.

Duran, J., Saez, I., Gruart, A., Guinovart, J.J., and Delgado-Garcia, J.M. (2013). Impairment in long-term memory formation and learning-dependent synaptic plasticity in mice lacking glycogen synthase in the brain. J. Cereb. Blood Flow Metab. *33*, 550–556.

Elias, L.A.B., Wang, D.D., and Kriegstein, A.R. (2007). Gap junction adhesion is necessary for radial migration in the neocortex. Nature *448*, 901–907.

Ellefsen, K.L., Settle, B., Parker, I., and Smith, I.F. (2014). An algorithm for automated detection, localization and measurement of local calcium signals from camera-based imaging. Cell Calcium *56*, 147–156.

Escartin, C., Galea, E., Lakatos, A., O'Callaghan, J.P., Petzold, G.C., Serrano-Pozo, A., Steinhäuser, C., Volterra, A., Carmignoto, G., Agarwal, A., et al. (2021). Reactive astrocyte nomenclature, definitions, and future directions. Nat. Neurosci. *24*, 312–325.

Fernandes, D., and Carvalho, A.L. (2016). Mechanisms of homeostatic plasticity in the excitatory synapse. J. Neurochem. *139*, 973–996.

Garcia, A.D.R., Doan, N.B., Imura, T., Bush, T.G., and Sofroniew, M.V. (2004). GFAP-expressing progenitors are the principal source of constitutive neurogenesis in adult mouse forebrain. Nat. Neurosci. *7*, 1233–1241.

Ghézali, G., Calvo, C.-F., Pillet, L.-E., Llense, F., Ezan, P., Pannasch, U., Bemelmans, A.-P., Manneville, S.E., and Rouach, N. (2018). Connexin 30 controls astroglial polarization during postnatal brain development. Development *145*, dev155275.

Giaume, C., Koulakoff, A., Roux, L., Holcman, D., and Rouach, N. (2010). Astroglial networks: a step further in neuroglial and gliovascular interactions. Nat. Rev. Neurosci. *11*, 87–99.

Glück, C., Ferrari, K.D., Binini, N., Keller, A., Saab, A.S., Stobart, J.L., and Weber, B. (2021). Distinct signatures of calcium activity in brain mural cells. Elife *10*, e70591.

Goulart, B.K., de Lima, M.N.M., de Farias, C.B., Reolon, G.K., Almeida, V.R., Quevedo, J., Kapczinski, F., Schröder, N., and Roesler, R. (2010). Ketamine impairs recognition memory consolidation and prevents learning-induced increase in hippocampal brain-derived neurotrophic factor levels. Neuroscience *167*, 969–973.

Griemsmann, S., Höft, S.P., Bedner, P., Zhang, J., Von Staden, E., Beinhauer, A., Degen, J., Dublin, P., Cope, D.W., Richter, N., et al. (2015). Characterization of panglial gap junction networks in the thalamus, neocortex, and hippocampus reveals a unique population of glial cells. Cereb. Cortex. *25*, 3420–3433.

Guyenet, S.J., Furrer, S.A., Damian, V.M., Baughan, T.D., La Spada, A.R., and Garden, G.A. (2010). A simple composite phenotype scoring system for evaluating mouse models of cerebellar ataxia. J. Vis. Exp., 1787. https://doi.org/10.3791/1787.

Habbas, S., Santello, M., Becker, D., Stubbe, H., Zappia, G., Liaudet, N., Klaus, F.R., Kollias, G., Fontana, A., Pryce, C.R., et al. (2015). Neuroinflammatory TNFα impairs memory via astrocyte signaling. Cell *163*, 1730–1741.

Henneberger, C., Papouin, T., Oliet, S.H.R., and Rusakov, D.A. (2010). Long-term potentiation depends on release of D-serine from astrocytes. Nature *463*, 232–236.

Hickman, S.E., Kingery, N.D., Ohsumi, T.K., Borowsky, M.L., Wang, L.C., Means, T.K., and El Khoury, J. (2013). The microglial sensome revealed by direct RNA sequencing. Nat. Neurosci. *16*, 1896–1905.

Hughes, C.S., Foehr, S., Garfield, D.A., Furlong, E.E., Steinmetz, L.M., and Krijgsveld, J. (2014). Ultrasensitive proteome analysis using paramagnetic bead technology. Mol. Syst. Biol. *10*, 757.

Jahn, H.M., Kasakow, C.V., Helfer, A., Michely, J., Verkhratsky, A., Maurer, H.H., Scheller, A., and Kirchhoff, F. (2018). Refined protocols of tamoxifen injection for inducible DNA recombination in mouse astroglia. Sci. Rep. *8*, 5913.

Keren-Shaul, H., Spinrad, A., Weiner, A., Matcovitch-Natan, O., Dvir-Szternfeld, R., Ulland, T.K., David, E., Baruch, K., Lara-Astaiso, D., Toth, B., et al. (2017). A unique microglia type associated with restricting development of Alzheimer's disease. Cell *169*, 1276–1290.e17.

Kettenmann, H., Kirchhoff, F., and Verkhratsky, A. (2013). Microglia: new roles for the synaptic stripper. Neuron *77*, 10–18.

Ko, M.C., Lee, M.C., Amstislavskaya, T.G., Tikhonova, M.A., Yang, Y.-L., and Lu, K.-T. (2014). Inhibition of NKCC1 attenuated hippocampal LTP formation and inhibitory avoidance in rat. PLoS One *9*, e106692.

Krasemann, S., Madore, C., Cialic, R., Baufeld, C., Calcagno, N., El Fatimy, R., Beckers, L., O'Loughlin, E., Xu, Y., Fanek, Z., et al. (2017). The TREM2-APOE pathway drives the transcriptional phenotype of dysfunctional microglia in neurodegenerative diseases. Immunity *47*, 566–581.e9.

Kunze, A., Congreso, M.R., Hartmann, C., Wallraff-Beck, A., Hüttmann, K., Bedner, P., Requardt, R., Seifert, G., Redecker, C., Willecke, K., et al. (2009). Connexin expression by radial glia-like cells is required for neurogenesis in the adult dentate gyrus. Proc. Natl. Acad. Sci. U S A *106*, 11336–11341.

Lagos-Cabré, R., Burgos-Bravo, F., Avalos, A.M., and Leyton, L. (2019). Connexins in astrocyte migration. Front. Pharmacol. *10*, 1546.

Larson, V.A., Mironova, Y., Vanderpool, K.G., Waisman, A., Rash, J.E., Agarwal, A., and Bergles, D.E. (2018). Oligodendrocytes control potassium accumulation in white matter and seizure susceptibility. Elife *7*, e34829.

Leger, M., Quiedeville, A., Bouet, V., Haelewyn, B., Boulouard, M., Schumann-Bard, P., and Freret, T. (2013). Object recognition test in mice. Nat. Protoc. *8*, 2531–2537.

Lenth, R., Singmann, H., Love, J., Buerkner, P., and Herve, M. (2019). Emmeans: Estimated Marginal Means, Aka Least-Squares Means (Cran.r-Project.Org).

Leutert, M., Rodríguez-Mias, R.A., Fukuda, N.K., and Villén, J. (2019). R2-P2 rapid-robotic phosphoproteomics enables multidimensional cell signaling studies. Mol. Syst. Biol. *15*, 1–20.

Li, W., Xu, X., and Pozzo-Miller, L. (2016). Excitatory synapses are stronger in the hippocampus of Rett syndrome mice due to altered synaptic trafficking of AMPA-type glutamate receptors. Proc. Natl. Acad. Sci. U S A *113*, E1575–E1584.

Liao, D., Scannevin, R.H., and Huganir, R. (2001). Activation of silent synapses by rapid activity-dependent synaptic recruitment of AMPA receptors. J. Neurosci. *21*, 6008–6017.

Liao, Y., Wang, J., Jaehnig, E.J., Shi, Z., and Zhang, B. (2019). WebGestalt 2019: gene set analysis toolkit with revamped UIs and APIs. Nucleic Acids Res. *47*, W199–W205.

Liddelow, S.A., Guttenplan, K.A., Clarke, L.E., Bennett, F.C., Bohlen, C.J., Schirmer, L., Bennett, M.L., Münch, A.E., Chung, W., Peterson, T.C., et al. (2017). Neurotoxic reactive astrocytes are induced by activated microglia. Nature *541*, 481–487.

Liddelow, S.A., Marsh, S.E., and Stevens, B. (2020). Microglia and astrocytes in disease: dynamic duo or partners in crime? Trends Immunol. *41*, 820–835.

Looser, Z.J., Barrett, M.J.P., Hirrlinger, J., Weber, B., and Saab, A.S. (2018). Intravitreal AAV-delivery of genetically encoded sensors enabling simultaneous two-photon imaging and electrophysiology of optic nerve axons. Front. Cell. Neurosci. *12*, 377.

Lutz, S.E., Zhao, Y., Gulinello, M., Lee, S.C., Raine, C.S., and Brosnan, C.F. (2009). Deletion of astrocyte connexins 43 and 30 leads to a dysmyelinating phenotype and hippocampal CA1 vacuolation. J. Neurosci. *29*, 7743–7752.

Madisen, L., Garner, A.R., Shimaoka, D., Chuong, A.S., Klapoetke, N.C., Li, L., van der Bourg, A., Niino, Y., Egolf, L., Monetti, C., et al. (2015). Transgenic mice

for intersectional targeting of neural sensors and effectors with high specificity and performance. Neuron *85*, 942–958.

Magistretti, P.J., and Allaman, I. (2018). Lactate in the brain: from metabolic end-product to signalling molecule. Nat. Rev. Neurosci. *19*, 235–249.

Magnotti, L.M., Goodenough, D.A., and Paul, D.L. (2011). Functional heterotypic interactions between astrocyte and oligodendrocyte connexins. Glia *59*, 26–34.

Mayrhofer, J.M., Haiss, F., Haenni, D., Weber, S., Zuend, M., Barrett, M.J.P., Ferrari, K.D., Maechler, P., Saab, A.S., Stobart, J.L., et al. (2015). Design and performance of an ultra-flexible two-photon microscope for *in vivo* research. Biomed. Opt. Express *6*, 4228.

Mederos, S., and Perea, G. (2019). GABAergic-astrocyte signaling: a refinement of inhibitory brain networks. Glia *67*, 1842–1851, glia.23644.

Menichella, D.M., Goodenough, D.A., Sirkowski, E., Scherer, S.S., and Paul, D.L. (2003). Connexins are critical for normal myelination in the CNS. J. Neurosci. *23*, 5963–5973.

Menichella, D.M., Majdan, M., Awatramani, R., Goodenough, D.A., Sirkowski, E., Scherer, S.S., and Paul, D.L. (2006). Genetic and physiological evidence that oligodendrocyte gap junctions contribute to spatial buffering of potassium released during neuronal activity. J. Neurosci. *26*, 10984–10991.

Meyer, N., Richter, N., Fan, Z., Siemonsmeier, G., Pivneva, T., Jordan, P., Steinhäuser, C., Semtner, M., Nolte, C., and Kettenmann, H. (2018). Oligodendrocytes in the mouse corpus callosum maintain axonal function by delivery of glucose. Cell Rep. *22*, 2383–2394.

Möbius, W., Cooper, B., Kaufmann, W.A., Imig, C., Ruhwedel, T., Snaidero, N., Saab, A.S., and Varoqueaux, F. (2010). Electron microscopy of the mouse central nervous system. Methods Cell Biol. *96*, 475–512.

Mori, T., Tanaka, K., Buffo, A., Wurst, W., Kühn, R., and Götz, M. (2006). Inducible gene deletion in astroglia and radial glia-A valuable tool for functional and lineage analysis. Glia *54*, 21–34.

Morrison, B.M., Lee, Y., and Rothstein, J.D. (2013). Oligodendroglia: metabolic supporters of axons. Trends Cell Biol. *23*, 644–651.

Moser, E.I., Krobert, K.A., Moser, M.B., and Morris, R.G. (1998). Impaired spatial learning after saturation of long-term potentiation. Science *281*, 2038–2042.

Murphy-Royal, C., Johnston, A.D., Boyce, A.K.J., Diaz-Castro, B., Institoris, A., Peringod, G., Zhang, O., Stout, R.F., Spray, D.C., Thompson, R.J., et al. (2020). Stress gates an astrocytic energy reservoir to impair synaptic plasticity. Nat. Commun. *11*, 2014.

Nagai, J., Rajbhandari, A.K., Gangwani, M.R., Hachisuka, A., Coppola, G., Masmanidis, S.C., Fanselow, M.S., and Khakh, B.S. (2019). Hyperactivity with disrupted attention by activation of an astrocyte synaptogenic cue. Cell *177*, 1280–1292.e20.

Nagai, J., Yu, X., Papouin, T., Cheong, E., Freeman, M.R., Monk, K.R., Hastings, M.H., Haydon, P.G., Rowitch, D., Shaham, S., et al. (2021). Behaviorally consequential astrocytic regulation of neural circuits. Neuron *109*, 576–596.

Oberheim, N.A., Tian, G.-F., Han, X., Peng, W., Takano, T., Ransom, B., and Nedergaard, M. (2008). Loss of astrocytic domain organization in the epileptic brain. J. Neurosci. *28*, 3264–3276.

Orthmann-Murphy, J.L., Freidin, M., Fischer, E., Scherer, S.S., and Abrams, C.K. (2007). Two distinct heterotypic channels mediate gap junction coupling between astrocyte and oligodendrocyte connexins. J. Neurosci. *27*, 13949–13957.

Pannasch, U., and Rouach, N. (2013). Emerging role for astroglial networks in information processing: from synapse to behavior. Trends Neurosci. *36*, 405–417.

Pannasch, U., Vargova, L., Reingruber, J., Ezan, P., Holcman, D., Giaume, C., Sykova, E., and Rouach, N. (2011). Astroglial networks scale synaptic activity and plasticity. Proc. Natl. Acad. Sci. U S A *108*, 8467–8472.

Pannasch, U., Derangeon, M., Chever, O., and Rouach, N. (2012). Astroglial gap junctions shape neuronal network activity. Commun. Integr. Biol. *5*, 248–254.

Pannasch, U., Freche, D., Dallérac, G., Ghézali, G., Escartin, C., Ezan, P., Cohen-Salmon, M., Benchenane, K., Abudara, V., Dufour, A., et al. (2014). Connexin 30 sets synaptic strength by controlling astroglial synapse invasion. Nat. Neurosci. *17*, 549–558.

Papouin, T., Dunphy, J.M., Tolman, M., Dineley, K.T., and Haydon, P.G. (2017). Septal cholinergic neuromodulation tunes the astrocyte-dependent gating of hippocampal NMDA receptors to wakefulness. Neuron *94*, 840–854.e7.

Pavlov, I., Savtchenko, L.P., Kullmann, D.M., Semyanov, A., and Walker, M.C. (2009). Outwardly rectifying tonically active GABAA receptors in pyramidal cells modulate neuronal offset, not gain. J. Neurosci. *29*, 15341–15350.

Perez-Riverol, Y., Bai, J., Bandla, C., García-Seisdedos, D., Hewapathirana, S., Kamatchinathan, S., Kundu, D.J., Prakash, A., Frericks-Zipper, A., Eisenacher, M., et al. (2022). The PRIDE database resources in 2022: a hub for mass spectrometry-based proteomics evidences. Nucleic Acids Res. *50*, D543–D552.

Pologruto, T.A., Sabatini, B.L., and Svoboda, K. (2003). ScanImage: flexible software for operating laser scanning microscopes. Biomed. Eng. Online *2*, 13.

Rash, J.E. (2010). Molecular disruptions of the panglial syncytium block potassium siphoning and axonal saltatory conduction: pertinence to neuromyelitis optica and other demyelinating diseases of the central nervous system. Neuroscience *168*, 982–1008.

Reichenbach, N., Delekate, A., Plescher, M., Schmitt, F., Krauss, S., Blank, N., Halle, A., and Petzold, G.C. (2019). Inhibition of Stat3-mediated astrogliosis ameliorates pathology in an Alzheimer's disease model. EMBO Mol. Med. *11*, e9665.

Ribeiro, C.S., Reis, M., Panizzutti, R., de Miranda, J., and Wolosker, H. (2002). Glial transport of the neuromodulator D-serine. Brain Res. *929*, 202–209.

Ritchie, M.E., Phipson, B., Wu, D., Hu, Y., Law, C.W., Shi, W., and Smyth, G.K. (2015). Limma powers differential expression analyses for RNA-sequencing and microarray studies. Nucleic Acids Res. *43*, e47.

Romanos, J., Benke, D., Saab, A.S., Zeilhofer, H.U., and Santello, M. (2019). Differences in glutamate uptake between cortical regions impact neuronal NMDA receptor activation. Commun. Biol. *2*, 127.

Rothhammer, V., Borucki, D.M., Tjon, E.C., Takenaka, M.C., Chao, C.-C., Ardura-Fabregat, A., de Lima, K.A., Gutiérrez-Vázquez, C., Hewson, P., Staszewski, O., et al. (2018). Microglial control of astrocytes in response to microbial metabolites. Nature *557*, 724–728.

Rouach, N., Avignone, E., Mème, W., Koulakoff, A., Venance, L., Blomstrand, F., and Giaume, C. (2002). Gap junctions and connexin expression in the normal and pathological central nervous system. Biol. Cell. *94*, 457–475.

Rouach, N., Koulakoff, A., Abudara, V., Willecke, K., and Giaume, C. (2008). Astroglial metabolic networks sustain hippocampal synaptic transmission. Science *322*, 1551–1555.

Ruminot, I., Gutiérrez, R., Peña-Münzenmayer, G., Añazco, C., Sotelo-Hitschfeld, T., Lerchundi, R., Niemeyer, M.I., Shull, G.E., and Barros, L.F. (2011). NBCe1 mediates the acute stimulation of astrocytic glycolysis by extracellular K+. J. Neurosci. *31*, 14264–14271.

Ruminot, I., Schmälzle, J., Leyton, B., Barros, L.F., and Deitmer, J.W. (2019). Tight coupling of astrocyte energy metabolism to synaptic activity revealed by genetically encoded FRET nanosensors in hippocampal tissue. J. Cereb. Blood Flow Metab. *39*, 513–523.

Saab, A.S., Neumeyer, A., Jahn, H.M., Cupido, A., Simek, A.A.M., Boele, H.-J., Scheller, A., Le Meur, K., Gotz, M., Monyer, H., et al. (2012). Bergmann glial AMPA receptors are required for fine motor coordination. Science *337*, 749–753.

Saab, A.S., Tzvetanova, I.D., and Nave, K.A. (2013). The role of myelin and oligodendrocytes in axonal energy metabolism. Curr. Opin. Neurobiol. *23*, 1065–1072.

Saab, A.S., Tzvetavona, I.D., Trevisiol, A., Baltan, S., Dibaj, P., Kusch, K., Möbius, W., Goetze, B., Jahn, H.M., Huang, W., et al. (2016). Oligodendroglial NMDA receptors regulate glucose import and axonal energy metabolism. Neuron *91*, 119–132.

Salter, M.W., and Stevens, B. (2017). Microglia emerge as central players in brain disease. Nat. Med. *23*, 1018–1027.

Santello, M., Toni, N., and Volterra, A. (2019). Astrocyte function from information processing to cognition and cognitive impairment. Nat. Neurosci. *22*, 154–166.

Schindelin, J., Arganda-Carreras, I., Frise, E., Kaynig, V., Longair, M., Pietzsch, T., Preibisch, S., Rueden, C., Saalfeld, S., Schmid, B., et al. (2012). Fiji: an open-source platform for biological-image analysis. Nat. Methods *9*, 676–682.

Schmued, L.C., Albertson, C., and Slikker, W. (1997). Fluoro-Jade: a novel fluorochrome for the sensitive and reliable histochemical localization of neuronal degeneration. Brain Res. *751*, 37–46.

Semyanov, A., Henneberger, C., and Agarwal, A. (2020). Making sense of astrocytic calcium signals - from acquisition to interpretation. Nat. Rev. Neurosci. *21*, 551–564.

Shigetomi, E., Jackson-Weaver, O., Huckstepp, R.T., O'Dell, T.J., and Khakh, B.S. (2013). TRPA1 channels are regulators of astrocyte basal calcium levels and long-term potentiation via constitutive D-serine release. J. Neurosci. *33*, 10143–10153.

Shih, A.Y., Blinder, P., Tsai, P.S., Friedman, B., Stanley, G., Lyden, P.D., and Kleinfeld, D. (2013). The smallest stroke: occlusion of one penetrating vessel leads to infarction and a cognitive deficit. Nat. Neurosci. *16*, 55–63.

Stehberg, J., Moraga-Amaro, R., Salazar, C., Becerra, A., Echeverría, C., Orellana, J.A., Bultynck, G., Ponsaerts, R., Leybaert, L., Simon, F., et al. (2012). Release of gliotransmitters through astroglial connexin 43 hemichannels is necessary for fear memory consolidation in the basolateral amygdala. FASEB J. *26*, 3649–3657.

Stellwagen, D., and Malenka, R.C. (2006). Synaptic scaling mediated by glial TNF-α. Nature *440*, 1054–1059.

Stobart, J.L., Ferrari, K.D., Barrett, M.J.P., Gluck, C., Stobart, M.J., Zuend, M., and Weber, B. (2018a). Cortical circuit activity evokes rapid astrocyte calcium signals on a similar timescale to neurons. Neuron *98*, 726–735 e4.

Stobart, J.L., Ferrari, K.D., Barrett, M.J.P., Stobart, M.J., Looser, Z.J., Saab, A.S., and Weber, B. (2018b). Long-term *in vivo* calcium imaging of astrocytes reveals distinct cellular compartment responses to sensory stimulation. Cereb. Cortex. *28*, 184–198.

Sunyer, B., Patil, S., Höger, H., and Luber, G. (2007). Barnes maze, a useful task to assess spatial reference memory in the mice. Protoc. Exch. https://doi.org/10.1038/nprot.2007.390.

Suzuki, A., Stern, S.A., Bozdagi, O., Huntley, G.W., Walker, R.H., Magistretti, P.J., and Alberini, C.M. (2011). Astrocyte-neuron lactate transport is required for long-term memory formation. Cell *144*, 810–823.

Teubner, B., Michel, V., Pesch, J., Lautermann, J., Cohen-Salmon, M., Söhl, G., Jahnke, K., Winterhager, E., Herberhold, C., Hardelin, J.-P., et al. (2003). Connexin30 (Gjb6)-deficiency causes severe hearing impairment and lack of endocochlear potential. Hum. Mol. Genet. *12*, 13–21.

Theis, M., Jauch, R., Zhuo, L., Speidel, D., Wallraff, A., Döring, B., Frisch, C., Söhl, G., Teubner, B., Euwens, C., et al. (2003). Accelerated hippocampal spreading depression and enhanced locomotory activity in mice with astrocyte-directed inactivation of connexin43. J. Neurosci. *23*, 766–776.

Theis, M., Söhl, G., Eiberger, J., and Willecke, K. (2005). Emerging complexities in identity and function of glial connexins. Trends Neurosci. *28*, 188–195.

Türker, C., Akal, F., Joho, D., Panse, C., Barkow-Oesterreicher, S., Rehrauer, H., and Schlapbach, R. (2010). B-fabric: the Swiss army knife for life sciences. In Adv. Database Technol. - EDBT 2010 - 13th Int. Conf. Extending Database Technol. Proc, pp. 717–720.

Vainchtein, I.D., and Molofsky, A.V. (2020). Astrocytes and microglia: in sickness and in health. Trends Neurosci. *43*, 144–154.

Wallraff, A., Köhling, R., Heinemann, U., Theis, M., Willecke, K., and Steinhäuser, C. (2006). The impact of astrocytic gap junctional coupling on potassium buffering in the hippocampus. J. Neurosci. *26*, 5438–5447.

Weber, B., and Barros, L.F. (2015). The astrocyte: powerhouse and recycling center. Cold Spring Harb. Perspect. Biol. *7*, a020396.

Wiencken-Barger, A.E., Djukic, B., Casper, K.B., and McCarthy, K.D. (2007). A role for Connexin43 during neurodevelopment. Glia *55*, 675–686.

Wolski, W.E., Panse, C., Grossmann, J., D'Errico, M., and Nanni, P. (2020). Prolfqua - R-Package for Proteomics Label Free Quantification (Poster, F1000Research). https://doi.org/10.7490/f1000research.1118455.1.

Wu, Y., Dissing-Olesen, L., MacVicar, B.A., and Stevens, B. (2015). Microglia: dynamic mediators of synapse development and plasticity. Trends Immunol. *36*, 605–613.

Yu, X., Taylor, A.M.W., Nagai, J., Golshani, P., Evans, C.J., Coppola, G., and Khakh, B.S. (2018). Reducing astrocyte calcium signaling *in vivo* alters striatal microcircuits and causes repetitive behavior. Neuron *99*, 1170–1187.e9.

Zhuo, L., Theis, M., Alvarez-Maya, I., Brenner, M., Willecke, K., and Messing, A. (2001). hGFAP-cre transgenic mice for manipulation of glial and neuronal function *in vivo*. Genesis *31*, 85–94.

Zuend, M., Saab, A.S., Wyss, M.T., Ferrari, K.D., Hösli, L., Looser, Z.J., Stobart, J.L., Duran, J., Guinovart, J.J., Barros, L.F., et al. (2020). Arousal-induced cortical activity triggers lactate release from astrocytes. Nat. Metab. *2*, 179–191.

STAR★METHODS

KEY RESOURCES TABLE

REAGENT or RESOURCE	SOURCE	IDENTIFIER
Antibodies		
rabbit polyclonal anti-Cx30 (IHC 1:500)	Thermo Fisher	Cat# 71-2200; RRID:AB_2533979
rabbit polyclonal anti-Cx43 (IHC 1:300)	Cell Signaling	Cat# 3512; RRID:AB_2294590
rabbit polyclonal anti-Iba1 (IHC 1:1000)	FUJIFILM Wako Chemicals	Cat# 019-19741; RRID:AB_839504
goat polyclonal anti-Iba1 (IHC 1:1000)	Abcam	Cat# ab5076; RRID:AB_2224402
rabbit polyclonal anti-P2Y12 (IHC 1:800)	AnaSpec	Cat# AS-55043A; RRID:AB_2298886
rat monoclonal anti-Clec7a (m-Dectin1; IHC 1:300)	InvivoGen	Cat# mabg-mdect; RRID:AB_2753143
rabbit polyclonal anti-GFAP (IHC 1:3000)	DAKO	Cat# Z334; RRID:AB_10013382
chicken polyclonal anti-GFAP (IHC 1:2000)	Abcam	Cat# ab4674; RRID:AB_304558
rabbit monoclonal anti-S100ß (IHC 1:700)	Abcam	Cat# ab52642; RRID:AB_882426
mouse monoclonal anti-NeuN (IHC 1:1000)	Chemicon	Cat# MAB 377; RRID:AB_2298772
rabbit polyclonal anti-MBP (IHC 1:1500; WB 1:500)	Merck Millipore	Cat# AB980; RRID:AB_92396
chicken polyclonal anti-Vimentin (IHC 1:3000)	Abcam	Cat# ab24525; RRID:AB_778824
IRDye 800CW goat anti-rabbit (WB 1:10'000)	LI-COR	P/N 926-32211; RRID AB_621843
Alexa Fluor 488-AffiniPure donkey anti-rabbit IgG (H+L) (IHC 1:700)	Jackson ImmunoResearch	Cat# 711-545-152; RRID:AB_2313584
Cy3-AffiniPure donkey anti-rabbit IgG (H+L) (IHC 1:700)	Jackson ImmunoResearch	Cat# 711-165-152; RRID:AB_2307443
Cy3-AffiniPure donkey anti-mouse IgG (H+L) (IHC 1:700)	Jackson ImmunoResearch	Cat# 711-165-151; RRID:AB_2315777
AffiniPure Fab fragment donkey anti-mouse IgG (H+L) (IHC 1:10)	Jackson ImmunoResearch	Cat# 715-007-003; RRID:AB_2307338
Bacterial and virus strains		
AAV-9/2-hGFAP-GCaMP6f (titer: 5.9 × 1012 VG/mL)	VVF, UZH, Zurich	Cat# v275-9; RRID:N/A
Chemicals, Peptides, and Recombinant Proteins		
Tamoxifen (100 mg/kg body weight, conc.: 10 mg/mL)	Sigma-Aldrich	Cat# T5648; RRID:N/A
Fluoro-Jade C (0.0001%)	Sigma-Aldrich	Cat# AG325; RRID:N/A
DAPI (stock: 1 mg/mL; use: 1:10'000)	Thermo Fisher	Cat# D3571; RRID:AB_2307445
TTX-citrate (1 μM)	Abcam	Cat# ab120055; RRID:N/A
NBQX disodium salt (10 μM)	Tocris Bioscience	Cat# 1044; Batch# 40; RRID:N/A
Biocytin (2 mg/mL)	Sigma-Aldrich	Cat# B4261; RRID:N/A
1(S),9(R)-(−)-Bicuculline methiodide (25 μM)	Sigma-Aldrich	Cat# 14343; RRID:N/A
HOT FIREPol EvaGreen qPCR Supermix	Solis BioDyne	Cat# 08-36; RRID:N/A
Revert 700 Total Protein Stain	LI-COR	Cat# P/N 926-11010; RRID:N/A
D-serine	Sigma-Aldrich	Cat# S4250; RRID:N/A
Critical Commercial Assays		
RNeasy Mini Kit	Qiagen	Cat# 74104; RRID:N/A
QuantiTect Reverse Transcription Kit	Qiagen	Cat# 205311; RRID:N/A

(*Continued on next page*)

Continued

REAGENT or RESOURCE	SOURCE	IDENTIFIER
Deposited Data		
Raw proteomics data	This paper	ProteomeXchange PRIDE; PXD031136
Experimental Models: Organisms/Strains		
Mouse: Slc1a3-CreERT2	(Mori et al., 2006)	MGI:3830051
Mouse: Cx30$^{fl/fl}$	(Boulay et al., 2013)	MGI:5486676
Mouse: Cx43$^{fl/fl}$	(Theis et al., 2003)	MGI:2445468; RRID:IMSR_EM:00327
Mouse: ROSA26-floxed-STOP-GCaMP6s (Ai96)	(Madisen et al., 2015)	JAX:024106; RRID:IMSR_JAX:024106
Software and Algorithms		
Clampfit 10.6 software	Molecular Devices	RRID:SCR_011323
Mini Analysis Program (version 6.0.7)	Synaptosoft Inc.	RRID:SCR_002184
Python programming language (version 3.6.2)	https://www.python.org	RRID:SCR_008394
Custom written motion tracking analysis	this paper	https://doi.org/10.5281/zenodo.5993391
ImageJ (Fiji, Version 2.1.0 /1.53c)	https://imagej.nih.gov/ij/index.html	(Schindelin et al., 2012); RRID:SCR_003070
Ilastik (version 1.3.0)	https://www.ilastik.org/	RRID:SCR_015246
R (version 3.6.1)	https://www.R-project.org/	RRID:SCR_001905
MATLAB (version R2017b)	MathWorks	RRID:SCR_001622
MATLAB toolbox CHIPS	Barrett et al., 2018	RRID:SCR_015741 https://github.com/EIN-lab/CHIPS
Other		
nitrocellulose blotting membrane (0.1 μm pore size)	Cytiva	Cat# 10600000; RRID:N/A
7900HT Fast Real-Time PCR System	Applied Biosystems	Cat# 4351405; RRID:N/A
Zirconium Oxide beads (0.5 mm)	Next Advance	Cat# ZROB05; RRID:N/A
Bullet Blender	Next Advance	BBX24
Tetric EvoFlow, Ivoclar Vivadent	Dema Dent AG	Cat#398594

RESOURCE AVAILABILITY

Lead contact

Further information and requests for resources and reagents should be directed to and will be fulfilled by the lead contact, Aiman S. Saab (asaab@pharma.uzh.ch).

Materials availability

Reagents are available upon request from the Lead Contact.

Data and code availability

The mass spectrometry proteomics data reported in this study (see also Table S1) have been deposited to the ProteomeXchange Consortium via the PRIDE (Perez-Riverol et al., 2022) partner repository and is publicly available as of the date of publication with the dataset identifier PXD031136. Code for calcium analysis toolbox CHIPS (Barrett et al., 2018) and motion tracking analysis are freely available on GitHub, as indicated in the key resources table. Any additional information required to reanalyze the data reported in this paper is available from the Lead Contact upon request.

EXPERIMENTAL MODEL AND SUBJECT DETAILS

All experimental procedures were approved by the local veterinary authorities according to the guidelines of the Swiss Animal Protection Law, Veterinary Office, Canton Zurich (Animal Welfare Act, 16 December 2005 and Animal Welfare Ordinance, 23 April 2008). Cx30$^{fl/fl}$: Cx43$^{fl/fl}$: GLAST$^{CreERT2/+}$ mice were generated by crossbreeding mice expressing the tamoxifen-sensitive Cre recombinase CreERT2 under the control of the murine *Slc1a3* (GLAST) promoter (Mori et al., 2006) with mice carrying floxed *Gjb6* (Cx30$^{fl/fl}$) (Boulay et al., 2013) and floxed *Gja1* (Cx43$^{fl/fl}$) (Theis et al., 2003) alleles. As controls, Cx30$^{fl/fl}$: Cx43$^{fl/fl}$: GLAST$^{+/+}$ littermates were used. Mice of either sex were used for experiments. The primer sequences used for genotyping were: for Cx30 flox; 5'-TTCCCTATGCTGGTA

GAGTGCTTGT-3' and 5'-GCAGTAACTTATTGAAACCCTTCACCT-3'; for Cx43 flox: 5'-GGGATACAGACCCTTGGACTCC-3' and 5'-TCACCCCAAGCTGACTCAACCG-3'; and for GLAST-CreERT2, 5'-GAGGCACTTGGCTAGGCTCTGAGGA-3' and 5'-GAGGA GATCCTGACCGATCAGTTGG-3' and 5'-GGTGTACGGTCAGTAAATTGGACAT-3'. For Cre reporter analysis, GLAST-CreERT2 mice were crossed with ROSA26-floxed-STOP-GCaMP6s (Ai96) reporter mice (Madisen et al., 2015) (JAX: 024106). Mice were kept on an inverted 12/12 hr light/dark cycle in standardized cages with food and water *ad libitum*.

METHOD DETAILS

Tamoxifen treatment

Tamoxifen treatment was performed as previously reported (Saab et al., 2012). Briefly, mice received daily intraperitoneal (i.p.) injections of tamoxifen at a dose of 100 mg/kg body weight for 5 consecutive days. Tamoxifen solution (10 mg/mL dissolved in corn oil) was always freshly prepared for each experimental cohort injected at the same time. Injections were performed in mice at the ages of 4-5 weeks (for acute slice experiments) or 8-12 weeks. Experiments were executed around 30 to 180 days post tamoxifen treatment, as specified in the text.

Immunohistochemistry and histology

Mice were anesthetized with pentobarbital and transcardially perfused with ice-cold 4% paraformaldehyde (PFA, Paraformaldehyde Granular, Electron Microscopy Sciences, Hatfield, PA) in phosphate-buffered saline (PBS, pH 7.4, (10X Dulbecco's)-Powder, Axon Lab AG, Baden-Dättwil, Switzerland) with a flow of 20 mL/min. Brains were dissected, halved coronally and post-fixed in 4% PFA for 3 hr at 4°C. Tissue was cryoprotected in 30% sucrose in PBS for ≈ 2 days at 4°C, and then stored at −80°C until needed for cutting. Coronal sections (40 μm) were cut using a microtome (Hyrax KS 34) and then stored in antifreeze solution (50 mM sodium phosphate buffer pH 7.4, 1 M glucose, 35% ethylene glycol and 3.5 mM sodium azide) at -20°C until further processing. Free floating sections were washed with 0.05% Triton X-100 (Sigma-Aldrich, Buchs, Switzerland) in Tris buffer (50 mM, pH 7.4) and then transferred to 0.3% Triton X-100 and 5% donkey serum in Tris buffer (blocking solution) for 1 hr at room temperature (RT). Sections were then incubated with primary antibodies diluted in blocking solution overnight at 4°C. See key resources table for a full list of antibodies used. For Cx30 labeling, before incubation in blocking solution, antigen retrieval was required and sections were heated (2 × 7 min) in sodium citrate buffer (10 mM, 0.05% Tween 20, pH 6) using a commercially available microwave (at 40% of full microwave power). For immunostainings involving primary antibodies raised in mouse, a pretreatment with anti-mouse IgG Fab fragments was performed. Fab fragments were added to the blocking solution and sections were preincubated overnight at 4°C. Following primary antibody incubation, sections were washed in Tris buffer and then incubated in Alexa Fluor 488- and Cy3-conjugated secondary antibodies for 45 min at RT. For nuclei labeling, DAPI (1:10000) was added to the secondary antibody solution. To evaluate gap junctional coupling in slices that were 4%-PFA fixed immediately after dye diffusion experiments, biocytin (Sigma-Aldrich) was visualized using Alexa Fluor 555-conjugated streptavidin (Thermo Fisher Scientific, Waltham, MA). Sections were mounted on SuperFrost Plus slides (Thermo Scientific) in Dako Fluorescence Mounting Medium (Dako, Jena, Germany).

For Fluoro-Jade C stainings, coronal brain slices (40 μm) were mounted on SuperFrost Plus slides, air-dried and then immersed in a solution containing 1% NaOH in 80% ethanol for 5 min. Slides were then rinsed with 70% ethanol (2 min) and in distilled water (2 min) before incubation in a 0.06% potassium permanganate (Sigma-Aldrich) solution for 10 min. Slides were then rinsed in distilled water before incubation in Fluoro-Jade C staining solution (0.0001% Fluoro-Jade C dye (Sigma-Aldrich) in 0.1% acetic acid solution) for 10 min. After washing in distilled water (3 × 1 min), slides were air-dried, cleared with xylene and coverslipped with Eukitt (Merck Millipore, Burlington, MA). Mice subjected to cortical microinfarcts caused by occlusion of penetrating arterioles (Shih et al., 2013) were used as positive controls to detect degenerating neurons.

For hematoxylin and eosin (H&E) stainings, post-fixed brains were embedded in paraffin and sagittal (2 μm) sections cut using a microtome. Sections were then deparaffinized, then rehydrated and successively incubated for 3-5 min in 0.1% hematoxylin (color blue; basic tissue compartments) and 0.1% eosin (color red, acidic tissue compartments).

Image acquisition and analysis

Confocal images were acquired using a Zeiss LSM 700 or Zeiss LSM 800 confocal laser scanning microscope equipped with a 10× (Plan-Apochromat, NA 0.45), a 25× (LCI Plan-Neofluar, NA 0.8) or a 40× objective (Plan-Apochromat, NA 1.4, Oil DIC (UV) VIS-IR). Whole brain section pictures of H&E-stained sections were taken with a Zeiss Axio Scan.Z1 slide scanner with a Plan-Apochromat 10× (NA 0.45) air objective and tiled images were automatically aligned with the built-in microscope software (ZEN software, Zeiss). Image analysis was performed with ImageJ (Fiji, Version 2.1.0/1.53 c; Schindelin et al., 2012) or Ilastik (Version 1.3.0). Confocal images present single plane and maximum intensity projections of z-stacks. For Cx30 and Cx43 expression analysis, fluorescent particles were counted after binarization of the images. For GFAP and Iba1 analysis, the fluorescent particle area was determined after binarization of the images using ImageJ. For cell density analysis, neurons ($NeuN^+$ cells) and microglia ($Iba1^+$ cells) were counted manually using the Cell Counter plugin in ImageJ. Astrocytes ($S100ß^+$ cells) were automatically counted using Ilastik. For Sholl analysis of astrocytes and microglia, maximum intensity projections were despeckled, binarized and analysis was performed using the Neuroanatomy Plugin (Legacy: Sholl analysis) in ImageJ with the first concentric circles set at 5.5 μm and 6 μm for astrocytes or microglia, respectively, and the subsequent concentric circles set with a radius step of 2 μm. For all analyses, at least 3 images from

each 3-4 brain sections from each 3-4 animals were analyzed. Pictures were taken in defined, comparable brain areas for all mice (using DAPI channel for selection), and the experimenter was blinded to the genotypes.

Real time quantitative PCR

Mice were deeply anesthetized with isoflurane, decapitated and brains quickly dissected on ice. Tissue was homogenized in RNeasy Lysis Buffer (RLT, Qiagen, Hilden, Germany) using 0.5 mm Zirconium Oxide beads (ZROB05, Next Advance, Troy, NY) and the tissue homogenizer Bullet Blender (BBX24, Next Advance; 2× 15 s cycles on setting 4). RNeasy Mini Kit (Qiagen) and QuantiTect Reverse Transcription Kit (Qiagen) were used for RNA isolation and cDNA synthesis, respectively, according to the manufacturer's instructions, including a genomic DNA removal step. Using EvaGreen (HOT FIREPol, Solis BioDyne, Tartu, Estonia) and an ABI 7900HT Fast Real-Time PCR System (Applied Biosystems, Foster City, CA), we performed real-time qPCR to quantify the relative loss of *Gjb6* and *Gja1* mRNA following gene recombination. The following primers were used for mRNA expression analysis: for *Gjb6* (5'-GGCCGAGTTGTGTTACCTGCT-3', 5'-TCTCTTTCAGGGCATGGTTGG-3'); for *Gja1* (5'-GGTGGACTGCTTCCTCTCAC-3', 5'-GAG CGAGAGACACCAAGGAC-3'). As endogenous gene controls *Actb*, *hprt* and *tbp* were used: for *Actb* (5'-CTTCCTCCCTGGAGAA GAGC-3', 5'-ATGCCACAGGATTCCATACC-3'), for *hprt* (5'-ACAGGCCAGACTTTGTTGGA-3', 5'-CACAAACGTGATTCAAAT CCCTGA-3') and for *tbp* (5'-CACAGGAGCCAAGAGTGAAGAA-3', 5'-GCTGGGAAGCCCAACTTCTG-3'). For each reaction three technical replicates were averaged per animal.

Western blotting

Tissue lysis was performed in RIPA buffer (150 mM NaCl, 0.1% Triton X-100, 0.5% sodium deoxycholate, 0.1% SDS, 50 mM Tris HCl, pH 8.0, and protease inhibitors (Roche, Basel, Switzerland)) using 0.5 mm Zirconium Oxide beads and the Bullet Blender tissue homogenizer. Protein concentration was determined by bicinchoninic acid analysis (BCA Protein Assay, Merck Millipore, Burlington, MA). Protein lysate (40 μg) was size-separated by SDS-PAGE on 12% (w/v) polyacrylamide gels and then transferred to a nitrocellulose blotting membrane (0.1 μm pore size, Amersham Protran, Cytiva, Washington, DC). Following a 1 hr incubation in blocking solution (5% Blocking Reagent (Roche) in PBS) membranes were probed overnight at 4 °C with rabbit anti-MBP antibody (1:500, Merck Millipore). After rinsing with 0.05% PBS-Tween, blots were incubated with IRDye 800CW anti-rabbit secondary antibody (1:10'000, LI-COR, Lincoln, NE) and infrared fluorescence was detected using an Odyssey Imaging System (Odyssey CLx, LI-COR). Normalization was performed by Revert 700 Total Protein Stain (LI-COR).

Electron microscopy and analysis

Following anesthesia using pentobarbital, mice were perfused with PBS (pH 7.4) and subsequently with fixative solution (4% PFA, 2.5% glutaraldehyde in phosphate buffer with 0.5% NaCl, pH 7.4). Brains and optic nerves were dissected and postfixed in the same fixative overnight at 4°C. Tissue preparation and electron microscopy was performed as previously described (Möbius et al., 2010). Briefly, for embedding, pieces of tissue were postfixed with 2% OsO4 (Science Services, Munich, Germany) in 0.1 M phosphate buffer pH 7.3 and embedded in EPON (Serva, Heidelberg, Germany) after dehydration with acetone. Ultrathin sections were prepared with a Leica UC7 ultramicrotome (Leica, Vienna, Austria) and stained with UranylLess™ (Science Services, Munich, Germany). EM pictures were taken with a Zeiss EM912 electron microscope (Carl Zeiss Microscopy GmbH, Oberkochen, Germany) using an on-axis 2k CCD camera (TRS, Moorenweis, Germany).

Image analysis was performed with ImageJ (Fiji, Version 2.0.0-rc-69/1.52). For g-ratio analysis, 6-7 random overview EM pictures (at 8000× magnification) from optic nerve sections were taken and 300-350 axons per animal were analyzed. G-ratios (axon diameter divided by the axon diameter including the myelin sheath) were determined from circular areas equivalent to the measured areas. For analysis of synaptic density in the CA1 stratum radiatum, synapses were counted in 5 randomly taken images (116.6 μm^2 areas) from coronal hippocampal sections per animal, and 3-5 animals were analyzed. Glutamatergic excitatory synapses were identified by their prominent postsynaptic densities (electron-dense material) of around 30 nm thickness. The experimenter was blinded to the images.

TMT-based proteomics analysis

Hippocampus tissue lysates were obtained as detailed for Western blotting. The TMT-based quantitative proteomics was performed by the Functional Genomics Center Zurich (FGCZ). Protein concentration was estimated using the Lunatic UV/Vis polychromatic spectrophotometer (Unchained Labs). For each sample 100 μg of proteins were taken and reduced with 2 mM TCEP (tris(2-carboxyethyl)phosphine) and alkylated with 15 mM iodoacetamide at 60°C for 30 min. Samples were prepared using the single-pot solid-phase enhanced sample preparation (SP3). The SP3 protein purification, digest and peptide clean-up were performed using a KingFisher Flex System (Thermo Fisher Scientific) and Carboxylate-Modified Magnetic Particles (GE Life Sciences; GE65152105050250, GE45152105050250; Hughes et al., 2014; Leutert et al., 2019). Beads were conditioned following the manufacturer's instructions, consisting of 3 washes with water at a concentration of 1 μg/μL. Samples were diluted with 100% ethanol to a final concentration of 60% ethanol. The beads, wash solutions and samples were loaded into 96 deep well- or micro-plates and transferred to the KingFisher. Following steps were carried out on the robot: collection of beads from the last wash, protein binding to beads (14 min), washing of beads in wash solutions 1-3 (80% ethanol, 3 min each), protein digestion (overnight at room temperature with a trypsin protein ratio of 1:50 in 50 mM Triethylammonium-bicarbonat (TEAB)) and peptide elution from the magnetic beads (water, 6 min). The digest solution and water elution were combined and dried to completeness.

For TMT-labeling, 200 μg TMT10plex reagent (Thermo Fisher Scientific, 90110) was dissolved in 41 μL of anhydrous acetonitrile (Sigma-Aldrich) and added to 45 μg peptides in 100 μL of 50 mM TEAB, pH 8.5. The solution was gently mixed and incubated for 60 min at room temperature. The reaction was quenched by adding 8 μl of 5% hydroxylamine (Thermo Fisher Scientific). The combined TMT sample was created by mixing equal amounts of each TMT channel together. Labeled peptides were offline pre-fractionated using high pH reveres phase chromatography. With an 80 min linear gradient from 5-40% acetonitrile 9 mM NH4HCO2, peptides were separated on a XBridge Peptide BEH C18 column (130 Å, 3.5 μm, 4.6 mm X 250 mm, Waters). Every minute a new fraction was collected and concatenated to 8 final fractions. These fractions were dried down and resuspended in 40 μL of 3% acetonitrile, 0.1% formic acid containing indexed retention time (iRT)-peptides (Biognosys).

Mass spectrometry analysis was performed on an Orbitrap Fusion Lumos (Thermo Scientific) equipped with a Digital PicoView source (New Objective) and coupled to a M-Class UPLC (Waters). Solvent composition of the two channels was 0.1% formic acid for channel A and 0.1% formic acid, 99.9% acetonirile for channel B. For each sample 600 ng of peptides were loaded on a commercial MZ Symmetry C18 Trap Column (100 Å, 5 μm, 180 μm × 20 mm, Waters) followed by nanoEase MZ C18 HSS T3 Column (100 Å, 1.8 μm, 75 μm × 250 mm, Waters). The peptides were eluted at a flow rate of 300 nl/min. After an initial hold at 5% B for 3 min, a gradient from 5 to 22% B in 80 min and 32% B in 10 min was applied. The column was washed with 95% B for 10 min and afterwards the column was re-equilibrated to starting conditions for additional 10 min. Samples were acquired in a randomized order. The mass spectrometer was operated in data-dependent mode (DDA) acquiring a full-scan MS spectra (375−1'500 m/z) at a resolution of 120'000 at 200 m/z after accumulation to a target value of 400'000. Data-dependent MS/MS were recorded in the Orbitrap using quadrupole isolation with a window of 0.7 Da and HCD fragmentation with 38% fragmentation energy. The Orbitrap was operated at 50'000 resolution with a target value of 100'000 and a maximum injection time of 105 ms. Only precursors with intensity above 50'000 were selected for MS/MS and the maximum cycle time was set to 3 s. Charge state screening was enabled. Singly, unassigned, and charge states higher than seven were rejected. Precursor masses previously selected for MS/MS measurement were excluded from further selection for 20 s, and the exclusion window was set at 10 ppm. The samples were acquired using internal lock mass calibration on m/z 371.1012 and 445.1200. The mass spectrometry proteomics data were handled using the local laboratory information management system (LIMS; Türker et al., 2010).

The acquired raw MS data were processed by Proteome Discoverer (PD version 2.4), followed by protein identification using the integrated Sequest HT search engine. Spectra were searched against the mus musculus reference proteome (downloaded from UniProt, 20190709), concatenated with common protein contaminants. Carbamidomethylation (C), TMT (+229.163Da; peptide N-term and K) were set as fixed modification, while methionine oxidation and N-terminal protein acetylation were set as variable. Enzyme specificity was set to trypsin allowing a minimal peptide length of 6 amino acids and a maximum of two missed-cleavages. PD default tolerance settings were applied. The maximum false discovery rate (FDR) for peptides was set to 0.01. For reporter ion quantification the integration tolerance was 20 ppm for the most confident peak. Protein fold changes were computed based on Intensity values reported in the Protein output. A set of functions implemented in the R package prolfqua (Wolski et al., 2020) was used to filter for proteins with two or more peptides. To normalize the data, we used a modified robust z-score transformation, which preserves the original variance of the data. To determine treatment differences we fitted the linear model to every protein, computed contrasts and moderated the variance, t-statistics, and p-values (Ritchie et al., 2015). False discovery rates were determined from p-values using Benjamini-Hochberg adjustment. In addition, we performed gene set enrichment analysis (GSEA) using the WEB-based GEne SeT AnaLysis Toolkit (webgestalt.org).

Acute brain slice preparation

Mice (3-5 months old) were anesthetized with isoflurane, decapitated, and brains were quickly dissected and placed in an ice-cold cutting solution containing (in mM): 130 K-gluconate, 15 KCl, 0.2 EGTA, 20 HEPES, and 25 glucose (pH 7.4 adjusted with NaOH). Transversal hippocampus slices (300-350 μm thick) were cut using a vibratome (Vibration microtome, HM 650V, VWR) and then briefly immersed for 1 min at RT in a solution containing (in mM): 225 D-mannitol, 25 glucose, 2.5 KCl, 1.25 NaH_2PO_4, 26 $NaHCO_3$, 0.8 $CaCl_2$, 8 $MgCl_2$ (pH 7.4). Slices were then transferred to an artificial cerebral spinal fluid (ACSF) solution composed of (in mM): 125 NaCl, 2.5 KCl, 25 $NaHCO_3$, 1.25 NaH_2PO_4, 2 $MgCl_2$, 1 $CaCl_2$, 25 glucose, maintained at 34°C for 30 min and then at RT thereafter. Solutions were continuously bubbled with 95% O_2 and 5% CO_2.

Electrophysiology and analysis

Hippocampal slices were transferred to a submerged recording chamber (RC-26, Warner Instruments, Hamden, CT) mounted on an upright Olympus microscope (BX61WI) equipped with differential interference contrast and were perfused with ACSF (containing in mM: 125 NaCl, 2.5 KCl, 25 $NaHCO_3$, 1.25 NaH_2PO_4, 2 $MgCl_2$, 2 $CaCl_2$, 25 glucose, saturated with 95% O_2 and 5% CO_2) maintained at 30°C by an in-line solution heater (TC-344C, Warner Instruments). Cells were visualized using a 40× water-immersion objective (LUMPlanFL/IR 40×/0.80 W, Olympus). Somatic whole-cell recordings were performed, without series resistance compensation, from CA1 pyramidal cells and stratum radiatum astrocytes, using 4-10 MΩ glass pipettes filled with (in mM): 135 K-gluconate, 4 KCl, 2 NaCl, 10 HEPES, 4 EGTA, 4 Mg-ATP, 0.3 Na-GTP (pH 7.3, adjusted with KOH); or for neuronal synaptic activity recordings (in mM): 8 NaCl, 145 $CsMeSO_3$, 10 HEPES, 10 Na_2-phosphocreatine, 2 Na_2-ATP, 0.5 Na-GTP, 0.3 EGTA, 5 lidocaine N-ethyl bromide (QX-314), and 10 TEA (pH 7.25 adjusted with CsOH). Astrocytes were identified by their small cell bodies, linear IV-curves, high resting potentials (around -80 mV) and low input resistance (around 20 MΩ). For intercellular coupling experiments, biocytin

(2 mg/mL, Sigma-Aldrich) was added to the internal solution and passive diffusion was limited to 20 min in current-clamp mode. Immediately after recordings, slices were fixed in 4% PFA for 12-24 hr and then processed for immunohistochemical analysis. Intrinsic properties of CA1 pyramidal neurons were measured in current clamp mode (in the absence of synaptic blockers) and depolarizing current injection steps of 500 ms duration were used to elicit action potentials and to measure the input-output relationship. For miniature excitatory postsynaptic current (mEPSC) recordings, cells were voltage-clamped at -70 mV in the presence of bicuculline-methiodide (25 μM, Sigma-Aldrich) and tetrodotoxin TTX (1 μM, Abcam, Cambridge, UK) in the bathing solution to block inhibitory input and neuronal spiking activity, respectively. Evoked EPSCs were induced by stimulating Schaffer collaterals in CA1 stratum radiatum using ACSF-filled theta glass electrodes placed 100-200 μm from recorded cells. Recordings were performed in the presence of 25 μM bicuculline-methiodide. Evoked AMPAR-mediated EPSCs were measured at −70 mV and the responses from 5 single pulses at 0.05 Hz were averaged per cell. Paired-pulse stimulations were performed with an interstimulus interval of 50 ms (averaging 5 paired-pulses, 20 s apart) and the ratio between the second and the first AMPA-EPSC peak amplitude was calculated. For recordings of evoked NMDAR-mediated EPSCs, cells were voltage-clamped at +40 mV and AMPARs were blocked by 10 μM 2,3-Dioxo-6-nitro-1,2,3,4-tetrahydrobenzo[*f*]quinoxaline-7-sulfonamide (NBQX, Tocris Bioscience, Bristol, UK) added to the ACSF. Evoked NMDAR-EPSCs were induced by single pulse stimulations (averaging 5 pulses, 20 s apart) and by high frequency stimulations (10 pulses at 50 Hz and 100 Hz, 20 s apart). NMDAR decay kinetics were measured by fitting a double exponential function from the current peak to the baseline (Cathala et al., 2000), and the weighted mean decay time constant was used to compare decay times between genotypes and stimulation frequencies. Extracellular field responses were induced by stimulating Schaffer collaterals using a theta electrode and field excitatory postsynaptic potentials (fEPSPs) were recorded with a glass pipette (1-2 MΩ) filled with ACSF and placed in CA1 stratum radiatum close to the pyramidal layer. Long-term potentiation (LTP) was induced by theta-burst stimulations consisting of three 2-s trains of brief 100 Hz pulses (each train was composed of 10 stimulus epochs delivered at 5 Hz and each epoch contained four pulses at 100 Hz) delivered 20 s apart. Before LTP induction, baseline recordings were performed at 0.03 Hz stimulations and stimulus intensity was adjusted to evoke 40-50% of the maximum fEPSP slope. The same recording parameters were used to record fEPSP responses up to 45 min after LTP initiation. For measuring synaptic potentiation by D-serine, NMDAR-mediated fEPSP responses were recorded in ACSF containing low Mg^{2+} concentration (0.2 mM), bicuculline-methiodide (25 μM) and NBQX (10 μM). Schaffer collaterals were electrically stimulated at 0.05 Hz and after a 10 min baseline recording exogenous D-Serine (50 μM) was bath-applied for 20 min. Slices were prepared at the same Zeitgeber time ZT16 each day (ZT0 being the onset of light for the animal), because extracellular D-Serine levels may fluctuate throughout the 24 h period (Papouin et al., 2017).

Recordings were acquired with a MultiClamp 700B amplifier (Axon Instruments, Union City, CA), low-pass filtered at 2 kHz, digitized at 20 kHz (using Digidata 1550B, Axon Instruments) and stored to disk using pClamp 10 software (Molecular Devices, Sunnyvale, CA). Data analysis was performed offline using Clampfit 10.6 software (Molecular Devices) and Mini Analysis Program (Synaptosoft Inc., Fort Lee, NJ, USA).

Behavioral experiments

For all behavioral testing and analyses, the experimenter was blinded to the genotypes. Experiments were performed in adult mice before and after tamoxifen treatment, as specified in the text. All behavioral tests were conducted during the dark (active) phase of the animals, between Zeitgeber time ZT14 and ZT20.

Sensorimotor scoring was performed by adapting a previous protocol (Guyenet et al., 2010) and mainly focusing on gait, ledge test, hindlimb clasping, thin (3 mm) and thick (6 mm) horizontal wire tests. Each test was individually scored between 0-3, or 0-4 for the horizontal wire tests, with a combined total score of 0-17 for all tests. Briefly, the following scoring parameters were used for each test: 1) Gait was assessed on a flat surface from behind the animal, i.e. facing away from experimenter; Score 0: mouse moves normally, body weight supported on all limbs, not shaking, abdomen not touching the ground; Score 1: shows a light tremor; Score 2: walks haltingly, feet point away from the body, uncoordinated walk (“duck feet”); Score 3: severe tremor, hesitant walk, drags abdomen and tail along the surface. 2) Ledge test was performed by placing the mouse on the edge of a cage starting with its forepaws; Score 0: mouse walks along the ledge without losing footing or balance, appears coordinated and descends into the cage using its forepaws; Score 1: minor slips while walking but otherwise coordinated; Score 2: mouse slips often with hindlimbs and minor shakes while walking; Score 3: severe shaking, unable to place hindlimbs on the edge, falls off the ledge or lands on its head when descending. 3) Hindlimb clasping was evaluated by lifting the mouse by its tail near the base for 10 s about 30-40 cm above a table; Score 0: hindlimbs are stretched out away from abdomen for 10 s; Score 1: one hindlimb is withdrawn towards the abdomen for at least 5 s; Score 2: both hindlimbs are partially withdrawn towards the abdomen for at least 5 s; Score 3: both hindlimbs are completely withdrawn for more than 5 s. 4) Horizontal wire tests were performed by placing the mouse with its forepaws on the center of a suspended wire (3 or 6 mm diameter, 30 cm above cushioned ground) and measuring the latency to fall; Score 0: falling after 30 s or reaching the bars at the side; Score 1: falling between 21 and 30 s. Score 2: falling between 11 and 20 s. Score 3: falling between 6 and 10 s. Score 4: falling between 1 and 5 s. Each paradigm was scored four times (two sessions on two consecutive days, same time of the day) and the average score of each test was used to calculate the sum of scores for every animal. Animals with higher score values showed sensorimotor deficits.

Novel object recognition memory was tested following a previous protocol (Leger et al., 2013). For the experiment, a custom-made box (W25 × D25 × H15 cm) with transparent Plexiglass walls was used and its position in the room was kept constant throughout the tests. Animals were handled before testing, allowed to explore the arena, and experiments were performed with dimmed lights to

ensure a stress-free environment. Then two identical objects were placed in the box, 5 cm away from the walls, and mice were given 10 min to familiarize with the objects. For the test sessions (3 h and 24 h post familiarization), one object was exchanged with a novel object placed at the same location, and mice could explore the objects for 5 min. The novel object differed in brightness, shape, color, and texture from the old object. All sessions were recorded with a GoPro camera (HERO4; at 2704 × 1520 resolution and 24 frames per s) for analysis. The time spent exploring the old and novel object was measured. Our definition of exploratory behavior of the objects only included nose-directed behavior at a distance $\leq$ 2 cm to the object. Random chewing, climbing, or leaning on the object was excluded. The ratio of the exploratory time of the novel object to the total exploratory time (old and novel objects) determined the recognition index.

Barnes maze test was performed to assess spatial learning and memory, adapted from earlier protocols (Sunyer et al., 2007). A custom-made Barnes maze table (105 cm diameter) with 22 holes (5 cm diameter, 6 cm apart) was used. All holes were closed from underneath the table, except for one escape (target) hole to which an escape box was attached. Visual and optical cues (in the room and on the table) were used for spatial orientation. Since experiments were performed with the same groups of mice before and after tamoxifen treatment, the table orientation, spatial guidance cues, and the target hole were changed completely between the timepoints to avoid potential memory recall. To increase the motivation of animals to search and find the escape hole, weak, aversive stimuli (buzzer, bright light and fan pointing to the table) were used. All behavioral sessions were recorded with a GoPro camera (HERO4). The complete paradigm comprised an initial adaption day (day 0), a 4-day spatial acquisition phase (day 1-4) followed by a final test day (day 5). On the adaptation day, each mouse was placed in the center of the table beneath a dark box for 10 s. The box was lifted as soon as the aversive stimuli were turned on. Once the mouse entered the escape hole (with gentle guidance) the stimuli were turned off and the mouse was allowed to rest in the escape box for 2 min. During the spatial acquisition days, the same procedure was performed but now mice had to find the escape hole on their own. Each mouse had three training sessions per day ($\approx$1 h between sessions) and the latencies to find the escape hole were recorded. Latency cutoff time was 180 s. The average latency per day was used for analysis. On test day 5, the escape hole was sealed like the other holes and mice were allowed to search for the target hole for 90 s. The number of head pokes into each hole were counted. Walking distance was assessed from video recordings and analyzed using a custom-written Python (v3.6.2) code (available at https://github.com/martinholub/motrack). Briefly, mouse location on the table was identified and segmented in each frame based on distinct HSV (hue, saturation, value) color profile spectra, and then tracked in consecutive frames with mean-shift algorithm, that identifies two corresponding objects in consecutive frames based on the probability of finding a bounding box with a similar HSV color profile. The centroid coordinates of the mouse were saved together with the timestamp for each frame, which allowed further analysis of motion, distance, and time to reach the escape hole.

Awake two-photon calcium imaging and data analysis

Head-post implantation, craniotomy, virus injection and cranial window implantation surgery were performed as described before (Glück et al., 2021; Stobart et al., 2018b; Zuend et al., 2020). In brief, animals were implanted with a metal head-post. Two days later, a 4 × 4 mm craniotomy was performed and 130 nL AAV-9/2-hGFAP-GCaMP6f (titer 5.9 × 10^{12} vector genomes/mL; Cat.: v275-9, Viral Vector Core Facility (VVF), University of Zurich) at depths of 400 μm and 200 μm below cortical surface was injected. A square, 170 μm thick Sapphire glass window was placed onto the dura mater and was sealed with dental cement (Tetric EvoFlow, Ivoclar Vivadent, Derma Dent AG). One week after surgery, animals were handled 2-3 times per day for a week in order to get familiarized with the experimenter. Then, animals were adapted to the head fixation box by restraining them via the implanted head-post several times a day, with a gradual increase in restraint from seconds up to several minutes. After a training period of 2–3 weeks, animals learned to sit still for the duration of the imaging session.

Two-photon imaging was performed using a custom-built laser scanning microscope (Mayrhofer et al., 2015) with a tunable pulsed laser (MaiTai HP system, Spectra-Physics) and equipped with a 20× (W Plan-Apochromat 20×/1.0 NA, Zeiss) water-immersion objective. During *in vivo* measurements, the animals were head-fixed. GCaMP6f was excited at 940 nm, and emission was detected with GaAsP photomultiplier modules (Hamamatsu Photonics) fitted with a 535/50 nm band-pass filter (Semrock). Control of microscope laser scanning was achieved with a customized version of ScanImage [r3.8.1; Janelia Research Campus; (Pologruto et al., 2003)]. At the beginning of each imaging period, a high resolution (512 × 512 pixels, 0.74 Hz) image was collected for reference and 3 min imaging sessions (128 × 128 pixels; 11.84 Hz) in multiple locations were collected with a zoom factor of 4, but overall imaging periods per day did not exceed more than 15 min per animal. Multiple imaging sessions were conducted on different days for each animal. Animals could recover for at least 48 h between subsequent imaging days.

Data processing and analysis was carried out with MATLAB (MathWorks, R2017b) and ImageJ. Calcium data were analyzed with a custom MATLAB toolbox (CHIPS; Barrett et al., 2018) as previously described (Stobart et al., 2018b; Zuend et al., 2020). In brief, soma regions of interest (ROIs) were selected manually in ImageJ and signals in astrocytic processes (microdomains) were automatically identified by an activity-based algorithm (Ellefsen et al., 2014). If a process domain centroid was within a soma ROI the detected process domain was excluded from the analysis. Data were corrected for x-y motion using a 2D-convolution engine. Traces were z-scored (10 iterations, threshold: 2*SD). Signal peaks were identified and measured using a band-pass filter (f1 = 0.025 Hz, f2 = 1 Hz) before running the MATLAB findpeaks function.

QUANTIFICATION AND STATISTICAL ANALYSIS

Statistical analyses were performed using R (versions 3.6.1 and 3.6.3) and GraphPad Prism (Version 8.4.2, Graphpad Software). We used the lme4 package for linear mixed effects models (lmer function of lme4: R package version 1.1.21; Bates et al., 2015). For histological analyses, we used *genotype* and *brainArea*, and where appropriate, *timepoint* as fixed effects. We added *picture* as a covariate and we allowed for random intercepts for the sections nested within animals (1|animal/section) as a random effect. Defining *picture* as a covariate was included when images were always taken in the same locations (e.g. picture1 in cortical layer II/III, picture2 in layer IV and picture3 in layer V/VI). For behavioral analyses, we used *genotype* and *timepoint*, and where appropriate, *experiment* or *testday* as fixed effects and we allowed for random intercepts for the animals (1|animalID). When inspection of residual plots revealed obvious deviations from homoscedasticity or normality, the response variable was log-transformed for statistical analysis. Values for differences between *genotypes* (and *timepoints*) were obtained post-hoc using the emmeans package with pairwise comparisons (R package version 1.4.4; Lenth et al., 2019). For log-transformed or non-transformed response variables, the ratio (r) or the difference (ß) between compared pairs, respectively, is stated in the figure legends. Also, where appropriate, multiple comparisons data were analyzed with two-way ANOVA and inter-group comparisons were made using a Mann Whitney U test, paired or unpaired student's t test, as indicated in the figure legends. Calcium data were analyzed using Mann Whitney U tests in R (wilcox.test() function). All data is presented as mean ± SEM. p values $\leq$ 0.05 were considered statistically significant and are stated together with each sample size in the figure legends. For whole-cell recordings, each recorded cell was considered a biological replicate. For extracellular LTP recordings, each brain slice was considered a biological replicate. Sample sizes were not determined in advance, since they were constrained by the availability of age-matched transgenic mouse cohorts.